國立臺灣大學電機資訊學院光電工程學研究所

碩士論文

Graduate Institute of Photonics and Optoelectronics
College of Electrical Engineering and Computer Science
National Taiwan University

Master Thesis

利用頻譜分析光學同調斷層掃瞄技術觀察癌細胞攝取過程中金奈米環之分佈

Observation of Au Nanoring Distribution during Cancer Cell Uptake with Spectroscopic Optical Coherence Tomography

李明駿

Ming-Jyun Li

指導教授：楊志忠博士

Advisor: C. C. Yang, Ph.D.

中華民國 103 年 7 月

July 2014

誌謝

能夠完成這本論文以及碩士學位，首先要感謝的人就是這兩年來辛苦指導我的教授楊志忠老師，除了專業知識外，更培養了我研究上該有的邏輯推演能力，以及做實驗必須之細心謹慎的態度，我要在此致上我的感謝。

其次要感謝的是江衍偉教授對於我研究過程中的指導與建議，使我得以改善並順利完成論文。在碩士班的這兩年，特別要感謝紀廷達學長在專業知識與實驗技能上的傳授，讓我有能力進行研究，且在我遇到困難時都願意協助我解決問題。

另外，這兩年在實驗室與我相處過的人們，紀廷達、杜毅洲、陳師揚、鞠之耕、褚哲寬、張祐維等，以及助理張佩、柯信鈺、尚音伶小姐都在各個方面給我許多協助，讓我在研究上更為順利。

最後，我要感謝我的母親，陳麗君女士，以及我的哥哥，李泰坤。感謝他們在我求學過程中的支持與陪伴，讓我一帆風順至現今得到碩士學位，十分感謝我的家人。結尾，我要感謝所有這一路上給過我幫助的所有人。

摘要

我們裝設一套頻域光學同調斷層掃描系統其光源頻寬約 200 奈米，在空氣中之縱向解析度可以達到約 2 微米，橫向解析度小於 4 微米。運用此光學同調斷層掃描系統掃描加入金奈米環後的兩種口腔癌細胞 (SCC4 和 SAS) 。金奈米環的侷域表面電漿子之共振行為，能提高光學同調斷層掃描影像訊號強度，我們將光學同調斷層掃描的光源頻譜均分成長波長和短波長兩部分，二者有不一樣之侷域表面電漿子共振強度。根據光學同調斷層掃描的頻譜分析技術，我們可以使長波長與短波長部分金奈米環分布在細胞樣品裡，產生不一樣的影像強度。光學同調斷層掃描呈現四個階段的細胞狀況，包括未加入金奈米環前、加入金奈米環後、清洗未貼附在細胞表面上或未為細胞吞噬金奈米環、及經過蝕刻貼附在細胞表面金奈米環。從光學同調斷層掃描的影像，尤其，從長波長與短波長的影像差異可以分辨貼附在細胞上之金奈米環和細胞吞噬之金奈米環。也觀察到連接抗體的金奈米環，其貼附細胞和為細胞吞噬效率變得更高。

Abstract

A spectral-domain optical coherence tomography (OCT) system with a light source of ~200 nm in spectral width to achieve the depth and lateral resolutions of ~2 and <4 microns, respectively, is built. This OCT system is used for scanning two kinds of human oral cancer cells (SCC4 and SAS) with applied Au nanorings (NRIs). The localized surface plasmon (LSP) resonance behavior of the Au NRIs, which results in strong scattering of the Au NRIs for OCT imaging, is well controlled such that the long- and short-wavelength halves of the OCT source spectrum have different LSP resonance strengths. Based on this spectral distribution, the spectroscopic operation of the OCT system can lead to the different imaging intensities of the Au NRI distribution in the cell solution between the long- and short-wavelength images. OCT scans are performed at four stages of cell solution, including those before the application of Au NRIs, after the application of Au NRIs, after the washout of the Au NRIs not adsorbed or internalized by the cells, and after the etching of the Au NRIs not internalized by the cells. From the OCT images, particularly the differences between the long- and short-wavelength images in the spectroscopic operation, one can identify the adsorbed and internalized Au NRIs by the cells. It is found that with antibody linkage to the Au NRIs, the Au NRI adsorption and internalization efficiencies become higher.

Contents

Chapter 1

Introduction

1.1 Optical Coherence Tomography

Optical Coherence Tomography (OCT) is a noninvasive, high-resolution imaging technique for biomedical applications [1, 2]. OCT can provide us with images of 1-15 μm resolution in the longitudinal direction, which is one to two orders of magnitude finer than the conventional ultrasound images method.Commercial OCT imaging rate can be as high as 100k A-scans per second [3-6]. OCT has been widely used in biomedical imaging, particularly in ophthalmology [6-11]. In dermatology, OCT has been implemented for the evaluation of the skin with burn damage [12-14]. OCT can also be used for scanning internal organs, such as colon, stomach, lung, and upper airway by integrating an OCT system with an endoscope [15-20]. Moreover, with a miniature catheter, imaging of intravascular and coronary artery diseases with OCT were reported [21-23]. In oral cancer study, the capability of OCT for imaging the underlying structures of both benign and malignant oral mucosa was demonstrated [24, 25]. Various approaches have been explored to find more contrast mechanisms for acquiring additional

information of tissue, including Doppler OCT [28, 29], polarization-sensitive OCT [30, 31], spectroscopic OCT [32, 33],and photo-thermal OCT [83, 84]. On the other hand, the use of gold nanoparticles such as nanospheres, nanocages, nanoshells, and nanorods with specific surface plasmon resonance (SPR) properties has been investigated. Au nanoparticles are promising as *in vivo* OCT contrast agents because they are biocompatible, easy to fabricate, and functional with additional modalities.

1.2 Theory of Optical Coherence Tomography

Basically, OCT represents a technique of low-coherence interferometry [1]. The interfered signals of a Michelson interferometer are directly related to the intensity distribution of backscattered light that reflects the in-depth structure of a sample. With a low-coherence (broadband) light source, either fluorescence-based or laser source, the allowed interference range (Coherence length) is small such that the imaging resolution in the depth direction is high. A scanning mechanism in the reference arm of the interferometer provides us with a means for fast axial imaging in a sample. Comparing with other microscopy techniques, because of the unique coherent gating nature, OCT has the advantages of higher signal-to-noise ratio and larger imaging depth. With the varieties in monitoring parameters, data collection, signal wavelength,

etc., many OCT configurations with specially designated terminologies have been introduced. The most fundamental configuration of OCT is the time-domain OCT (TD-OCT). Normally, a time-domain system consists of a Michelson interferometer. In the reference arm, to increase the axial scanning speed, an optical phase delay line (OPDL) is used for providing group delay and phase delay (for generating a modulation frequency) [34]. Usually, an OPDL includes a diffractive grating, a lens, and a galvanometer optical scanner for Fourier optics operation. The scanning frequency of an OPDL can be as high as several kHz. Fig. 1.1 shows the basic layout of an OCT system based on a Michelson interferometer. Here the light source is first split into the sample and reference arms through a beam splitter or a fiber coupler. The optical signals incident onto the sample are effectively backscattered from the tissue structures at different depths inside the sample. By modulating the optical path in the reference arm, the backscattered optical signals from the sample, which carry structure information, interfere with the optical signals reflected from the reference mirror. Then, the interfered signals are detected by a detector and transformed from the analog signal into digital signal through a data acquisition (DAQ) board. The sample structure can be reconstructed after software process. The signals detected by a detector can be expressed as

$$
\begin{aligned}
I_D(\tau) &= \left\langle \left| E_S(t) + E_R(t-\tau) \right|^2 \right\rangle \\
&= \left\langle \left| E_S(t) \right|^2 + \left| E_R(t-\tau) \right|^2 + E_S(t)^* E_R(t-\tau) + E_S{}^* E_R(t-\tau) \right\rangle \\
&= \left\langle \left| E_S(t) \right|^2 \right\rangle + \left\langle \left| E_R(t-\tau) \right|^2 \right\rangle + \left\langle 2\,\mathrm{Re}\, E_S(t) E_R{}^*(t-\tau) \right\rangle .
\end{aligned}
\tag{1-1}
$$

Here, E_S (t) and E_R (t-τ) represent the electric fields of the sample and reference arm, respectively. τ is the time delay between the sample and reference arms. E_S and E_R can be expressed as

$$
\begin{aligned}
E_S(t) &= E_{S0} e^{i\omega_0 t} \\
E_R(t-\tau) &= E_{R0} e^{i\omega_0 (t-\tau)} .
\end{aligned}
\tag{1-2}
$$

E_{S0} and E_{R0} represent the amplitudes of E_S (t) and E_R (t-τ), respectively. $\omega_0$is the optical angular frequency. By substituting Eq. (1-2) into Eq. (1-1), Eq. (1-1) can be rewritten as

$$
I_D(\tau) = E_{S0}{}^2 + E_{R0}{}^2 + 2E_{S0}E_{R0}\cos(\omega_0\tau). \tag{1-3}
$$

In Eq. (1-3), the first and second terms are DC components and the third term is the interference term, which contains the information of sample structure. Through a band-pass filter, the DC components can be removed and the depth information of sample structure can be obtained after Fourier transform. For a low-coherence light source, the electric field can be written as a function of spectral power density, S (ω). Therefore, the

E_S (t) and E_R (t-τ) are given by

$$E_S(t) = \frac{1}{2\pi}\int_{-\infty}^{\infty} S_S(\omega)e^{i\phi_S(\omega)}e^{i\omega t}d\omega$$

$$E_R(t-\tau) = \frac{1}{2\pi}\int_{-\infty}^{\infty} S_R(\omega)e^{i\phi_R(\omega)}e^{i\omega(t-\tau)}d\omega. \quad (1\text{-}4)$$

Here, $\phi_S(\omega)$ and $\phi_R(\omega)$ are the frequency-dependent phase values of the optical components in the sample and reference arms, respectively. By substituting Eq. (1-4) into Eq. (1-3), I_D (τ) can be expressed as

$$I_D(\tau) = \frac{1}{2\pi}\int_{-\infty}^{\infty} {S_S}^2(\omega)d\omega + \frac{1}{2\pi}\int_{-\infty}^{\infty} {S_R}^2(\omega)d\omega + \frac{1}{\pi}\int_{-\infty}^{\infty} S_S(\omega)S_R(\omega)e^{i\Delta\phi(\omega)}e^{i\omega\tau}d\omega \quad (1\text{-}5)$$

Here,△$\phi(\omega)$=｜$\phi_S(\omega)-\phi_R(\omega)$｜assuming that the spectral shape of the light source is a Gaussian-like spectrum and△ϕ (ω) = 0,S_S (ω) and S_R (ω) are given by

$$S_S(\omega) = S_{S0}e^{-\frac{2\ln 2(\omega-\omega_0)^2}{\Delta\omega^2}}$$

and

$$S_R(\omega) = S_{R0}e^{-\frac{2\ln 2(\omega-\omega_0)^2}{\Delta\omega^2}} \quad (1\text{-}6)$$

respectively. Here, I_D (ω) can be rewritten as

$$I_D(\tau) = I_S + I_R + \frac{S_{S0}S_{R0}\Delta\omega}{2\sqrt{\pi\ln 2}}e^{-\frac{\Delta\omega^2\tau^2}{16\ln 2}}\cos(\omega_0\tau)$$

$$= I_S + I_R + I_c e^{-\frac{4\ln 2\tau^2}{\Delta\tau^2}}\cos(\omega_0\tau),$$

where

$$I_C = \frac{S_{S0}S_{R0}\Delta\omega}{2\sqrt{\pi\ln 2}}, \qquad \Delta\tau = \frac{8\ln 2}{\Delta\omega}. \quad (1\text{-}7)$$

The optical path difference between the sample and reference arms, z, is equal to cτ /2, where c is the light speed. Therefore, the coherence length of light source,∆z, can be expressed as

$$\Delta z = \frac{C\Delta\tau}{2} = \frac{2\ln 2}{\pi}\left(\frac{\lambda_0^{\,2}}{\Delta\lambda}\right). \quad (1\text{-}8)$$

Here, λ_0 and $\triangle\lambda$ represent the central wavelength and the full-width at half-maximum (FWHM) of the light source spectrum. The coherence length of light source also represents the longitudinal resolution in the OCT system, which is inversely proportional to full-width at half-maximum of the light source spectrum and proportional to the square of the central wavelength.The other important factor of an OCT system is the transverse resolution, which depends on the beam diameter of the incident light before the focusing lens and the numerical aperture (NA) of the focusing lens in the sample arm. The lateral resolution of OCT operation is defined as the optical beam spot size focused onto the sample, which is given by

$$\Delta x = \frac{4\lambda f}{\pi d}. \quad (1\text{-}9)$$

Here, *f* is the focal length of the lens and *d* is the beam diameter before the lens. From Eq. (1-9), we can observe that a shorter focal length results

in better resolution. However, there is a tradeoff between the lateral resolution and the axial field-of-view. Fig. 1.2 depicts an optical beam focused by a lens. If the axial field-of-view is not large enough, the OCT image will be blurred in the region out of focus.

1.3 Fourier-domain Optical Coherence Tomography

In the TD-OCT, the depth information of a sample is acquired through the scanning with a galvanometer or other mechanical mechanisms in the reference arm. However, the imaging speed and the sensitivity of such an OCT system are limited by the mechanical mechanisms. Although the imaging speed can reach a few frames/sec with TD-OCT, it is not fast enough for clinical applications. The development of the spectral-domain OCT (SD-OCT) [35] or Fourier-domain OCT (FD-OCT) [36] greatly improved the imaging speed and the operation sensitivity [37-38]. The imaging speed of SD-OCT is higher than that of TD-OCT because of the mechanical depth scanning (A-mode scan) is unnecessary. In the SD-OCT or FD-OCT, the mechanical A-scan is replaced by a wavelength-resolving detectionscheme. The depth information of the sample can be obtained by measuring the interfered spectrum and performing an inverse Fourier transform. The imaging speed can be as high as several tens

frames/sec[39]. Such real-time or video-rate imaging is more suitable for clinical application.Based on the same fundamental principle of optical interferometry, the SD-OCT can be classified into two categories. In the first category, a broadband light source, such as a super-luminescence diode, is used and the interfered spectrum is detected by a spectrometer consisting of a diffraction grating, a Fourier transform lens, and a detector array or line-scan CCD. Although this method is good for 800-nm OCT, it is difficult to use such a scheme in the range of 1300 nm because the required detector arrays are not mature in this wavelength range [40]. In the second category, the swept-source OCT (SS-OCT) is widely used in the 1300 nm band [40, 41]. In an SS-OCT system, we detect the wavelength-resolved interfered spectrum by using a fast wavelength-scanning laser source and a single photo-detector. The SS-OCT has several major advantages over the first category of using a CCD. One of them is its higher robustness against sample motions because of its fast scanning mechanism [42]. The other advantage is the capability of separating the real OCT image from its mirror image [43]. Therefore, for obtaininghighquality OCT images in this research, we build SS-OCT systems to improve the imaging speed and sensitivity for research application.

1.3.1 Spectral-domain Optical Coherence Tomography

Fig.1.3 shows the setup of an SD-OCT system. The system configuration is similar to a time-domain OCT system except for the setup of the reference arm and the detection end. In the reference arm, the mechanical scanning mechanism is replaced by a fixed reflection mirror. In SD-OCT, the backscattered signals from the sample and the reference arms are obtained by a spectrometer instead of a detector. The spectrometer consists of a beam expander, a diffractive grating and a line-scan CCD (charge-coupled device). The beam diameter of the incident light is expanded by a telescope in order to obtain a better spectral resolution. Then the light is dispersed by the diffractive grating and collimated by an achromatic lens onto a line-scan CCD. The depth-resolved information can be extracted by an inverse Fourier-transform of the spectrum of the backscattered signal from the line-scan CCD. Although the imaging speed can be improved without mechanical scanning, there are some limitations in an SD-OCT system. First, the imaging speed is still limited by the acquisition rate of the line-scan CCD. A line-scan CCD with high acquisition rate will increase the cost of a system. Second, the technique of the line-scan CCD in the

1.3 μm is not mature. Therefore, it also limits the development of SD-OCT in the 1.3 μm band. Third, the motion artifact can be induced during the exposure time of the CCD. It will blur OCT images of SD-OCT system. In addition, a spectrometer is used in an SD-OCT system for the detection purpose. It increases the complexity of the system and the stability of the system becomes an issue.

1.3.2 Swept-source Optical Coherence Tomography

The other type of FD-OCT is SS-OCT. In an SS-OCT system, the use of a frequency-swept laser source eliminates the requirement of the spectrometer for detection purpose. Therefore, an SS-OCT system has several advantages over those of an SD-OCT system, including high robustness in system setup, higher imaging speed, and higher sensitivity. High-speed SS-OCT operation with a polygon-mirror tuning filter in the spectral range of 1.3μm has been implemented [3]. An SS-OCT system with the swept laser source near 1 μm in wavelength was also reported [44]. Such a system can reach a larger imaging depth, such as in the posterior eye, and is suitable for ophthalmic scanning in choroid study [45]. SS-OCT is particularly important for imaging in the wavelength ranges of 1 and 1.3 μm, in whichcharge-coupled devices (CCDs) or

detector arrays are not well developed yet. Although a swept laser source may have the problem of intensity fluctuation in output spectrum, the use of balanced detection has made the system noise of SS-OCT tremendously reduced. Fig.1.4 shows the setup of an SS-OCT system. Compared to the setup of SD-OCT system, the configuration of the SS-OCT system is much simpler. Although SS-OCT has many advantages including higher sensitivity, deeper imaging depth and high imaging speed, there are some limitations in the development of SS-OCT such as the swept-source and DAQ board.

Swept-source is a key component in an SS-OCT system.In a swept light source, semiconductor amplifier (SOA) is used as the gain medium and wavelength is swept in an external cavity with a polygon mirror or Fabry-Perot filter. Hence, the scanning rate of a swept-source is limited by the tuning speed of the polygon mirror or the Fabry-Perot filter. In general, the scanning rate of a commercial swept source is about 20 kHz. It is difficult to increase the speed due to the rotating-speed limit of the polygon mirror. In 2006, J. G. Fujimoto *et al.* proposed a new type of swept-source, i.e., Fourier-domain mode-locking laser (FDML), which can achieve a higher scanning rate as high as ten times that of a commercial swept source. Besides the scanning rate, it can provide higher output power, larger scanning depth and higher sensitivity [46].The

spectral range of a swept-source is equal to the amplified spontaneous emission (ASE) spectrum of an SOA. Unfortunately, it is difficult to find an SOA of even broader bandwidth. In general, the FWHM of ASE spectrum is below 120 nm in a commercial SOA. Another issue in an SS-OCT system is the speed of analog-to-digital conversion. As the scanning rate of a swept source increases, the speed of the DAQ board also needs to be increased.

1.4 Functional Imaging of OCT

1.4.1 Optical Doppler Tomography

The Doppler effect was discovered by Johann Christian Doppler in 1842. It describes the phenomenon of frequency change due to the relative motion between the wave source and detector. The Doppler ultrasound and laser Doppler flowmetry are the commonly used techniques for blood flow measurement based on the Doppler effect. The Doppler effect can also be monitored by an OCT system. Such a system provides the technique of optical Doppler tomography (ODT) [47, 48]. An ODT system can provide both structure image and blood flow velocity information simultaneously. It is quite useful for clinical applications which concern the blood flow and the distribution of

vessel.The Doppler phase shift $\Delta\Phi$ is given by

$$\Delta\Phi = \left(\vec{k}_s - \vec{k}_i\right)\cdot \bar{\mathrm{v}}. \qquad (1\text{-}10)$$

Here, $\vec{k}_s$ and $\vec{k}_i$ are the wave vectors of the scattered and incoming beam. $\bar{\mathrm{v}}$ is the velocity of moving object. We consider the backscattering case and define the angle between the incident beam and the blood flow direction as θ. Then,

$$\Delta\Phi = \frac{4\pi \mathrm{v}\cos\theta}{\lambda_0}. \qquad (1\text{-}11)$$

Here, λ_0 is the signal central wavelength. The phase-resolved optical Doppler tomography technique has been used for real-time imaging [49]. After Hilbert transformation, the phase change of the interference fringe can be obtained.

1.4.2 Polarization-sensitive OCT (PSOCT)

In biological tissue, there exists birefringence due to the ordered arrangement of muscle, tendons and nerves. By controlling the signal polarization of the OCT system, the sample birefringence property, which cannot be observed in an ordinary OCT image, can be obtained. Fig. 1.5 shows the setup of a PSOCT system.The system is basically a free-space Michelson interferometer designed to detect the variation of polarization

of the backscattered light from the sample. The input light is linearly polarized in the horizontal direction. The optical signal is split into the reference and sample arms with a beam splitter, BS. A quarter-wave plate QWP2 is placed in the reference arm with 22.5° orientation to provide the linearly polarized light with 45°orientation. In the sample arm, the horizontally polarized light is applied onto the sample. The polarizing beam splitter, PBS2, splits the recombined beams into two orthogonal polarization modes.

Finally, the signals are detected by two detectors to give the intensities for the horizontal (I_H) and vertical (I_V) components:

$$I_H(z) \propto R(z)\sin^2(k_0 z\Delta n). \quad (1\text{-}12)$$

$$I_V(z) \propto R(z)\cos^2(k_0 z\Delta n). \quad (1\text{-}13)$$

Here, *R (z)* is the backscattering intensity at depth *z*, Δn is the difference of reflective index between the fast and slow axes. The phase retardation is given by

$$\varphi(z) = \arctan\left[\left(\frac{I_V(z)}{I_H(z)}\right)^{1/2}\right] = k_0 z\Delta n. \quad (1\text{-}14)$$

Fig. 1.6 shows a PSOCT scanning image of porcine myocardium, in which part (a) shows the phase retardation image, and parts (b) and (c)

show the intensity images from both and single detector [50] backscattering.

1.4.3Photothermal OCT

Photothermal OCT is similar to traditional OCT but it requires a modulated photothermal excitation laser. Before the OCT light beam hits the sample, a dichroic mirror is used for combining the photothermal excitation laser with the OCT light beam. Both the OCT light beam and excitation laser are scanned and focused onto the sample at the same location.Fig.1.7 shows the basic layout of a photothermal OCT system.

The basic principle of photothermal OCT is the thermal expansionor refractive index change of tissue caused by the heating of the modulated laser.The induced optical path lengthvariation is measured with phase-sensitive OCT.The signal of a M-mode scan,*I (k,t)*,can be expressed as Eq. (1-15) with phase term,$\varphi(t)$,given by Eq. (1-16) :

$$I(k,t) = 2|E_s E_R| cos\{2k\Delta z + \varphi(t)\} \quad (1\text{-}15)$$

$$\varphi(t) = \frac{4\pi}{\lambda_0} A\sin(2\pi f_0 t) \quad (1\text{-}16)$$

InEq. (1-16),A represent the optical path length variation (OPLV)

produced by the thermal expansion refractive index change.$f_0$is the frequency of modulated excitation laser. $\lambda_0$is the central wavelength of the OCT light source. To obtain the OPLV, the signal of M-mode scan,*I (k,t)*, is Fourier transformed with respect to k and the phase term *φ (t)* can be obtained in Eq. (1-17), when the spatial frequency is selected to the z $=\Delta z$.

FT$[I(k,t)]_k$=$I(z,t)$

$$= [\delta(z-\Delta z)exp^{[-i\varphi(t)]} + \delta(z+\Delta z)exp^{[i\varphi(t)]} \qquad (1\text{-}17)$$

Similarly, the phase term *φ (t)* is Fourier transformed along t.TheOPLV is obtained in Eq. (1-18), when the temporal frequency is selected at $f=f_0$.

$$FT\,[\varphi(t)]_t = \frac{8\pi^2}{\lambda} A\left\{\frac{1}{2}[\delta(f-f_0)+\delta(f+f_0)]\right\} \quad (1\text{-}18)$$

Recently, this method has been applied to molecularimaging [51] by doping or injecting bio-marker which has a specific absorption property in the tissues for the measurementofoxygen saturation [52].

1.4.4 Spectroscopic OCT

Spectroscopic OCT is an extension of conventional OCT. It is based

on the concept that the optical properties of a tissue sample are dependent of the wavelength of light incidence. This image modality utilizes the broad bandwidth of a light source [32]. Because the broadsource spectrum may cover a range of wavelength-dependent variations of absorption, scattering,and other properties, OCT imagescan be provided with different spectral sections. For example, the absorption in the blood in mainly decided by the absorption of Hb and HbO_2. There is a cross-over behavior of the absorption spectra of Hb and HbO_2 around 800 nm in wavelength, which is shown is Fig. 1.8.The absorption coefficient of Hb is higher than HbO_2 in the wavelength range short than 800nm and is lower than HbO_2 beyond 800nm. If one can perform inverse Fourier transform of the spectrum interference signal in different parts of the spectrum range. The wavelength-dependent character of blood can be obtained.

1.5Using Metal Nanoparticles as Contrast Agent in OCT

OCT scanning uses the interfered backscattered coherent signal for retrieving sample structures. Therefore, any contrast agent, which can

enhance coherent backscattering, can be used for increasing OCT image quality. In this regard, the localized surface plasmon (LSP) resonance of a metal nanoparticle (NP) for producing strong coherent scattering is quite useful for OCT application. In particular, the use of bio-compatible Au NPs of proper bio-conjugation for targeting designated cells can lead to targeted OCT imaging, which is useful for the early diagnoses of cancer. Besides enhanced coherent backscattering, LSP resonance on metal NPs can also enhance absorption for increasing local temperature in a sample and hence changing its optical property such that signal features can be monitored by OCT scanning. In using Au NP as an OCT contrast agent, there are two possible methods. First, a light source with its spectrum different from the OCT scanning wavelength is used for exciting LSP resonance to change the local optical property of the sample such that this change can be monitored with OCT imaging. For instance, Au nanospheres with the LSP resonance wavelength around 532 nm and Au nanoshells with the LSP resonance wavelength around 808 nm have been used to generate heat in phantom samples through LSP-induced absorption and the temperature changes are monitored by OCT systems operated at 1300 nm [53, 54] and 840 nm [55]. In the second method, which is preferred, the OCT light source simultaneously excites LSP resonance and scans the sample. For such operation, the LSP resonance wavelength must coincide with the OCT spectral peak [56-62]. By using

Au nanospheres [56-57], nanoshells [60-62], nanorods [62], and nanocages [57, 58], the LSP resonance wavelength can be tuned to the range around 800 nm, which coincides with the OCT operation spectrum based on a super-luminescent diode. Due to the enhanced absorption through LSP resonance, temperature increases in phantoms [53-55, 58,59] and tissues [58] have been observed. Also, image contrast has been improved through enhanced backscattering of LSP resonance in phantoms and tissues [56, 57, 60-62]. It is noted that although quite many accomplishments of LSP-based OCT have been made, so far, the OCT operations with coincident LSP resonance and OCT light source spectra, which are preferred in practical applications, are limited to the spectral range of 800 nm. Because light penetration into bio-tissue can be deeper in the spectral range of 1300 nm, which is another commonly used spectral range for OCT operation, particularly for high-speed operation, an Au NP of 1300 nm in LSP resonance wavelength would be useful for further improving the OCT image quality. Although Au nanorods of large aspect ratios (>7) can push the LSP resonance wavelengths to reach 1200 nm, the uniformity and yield of such nanorods are quite low. This research team has successfully fabricated aqueous solution of Au nanorings (NRIs) with the LSP resonance wavelength tunable from 800 through 1300 nm based on nano-process techniques. Because of the high controllability of the fabrication procedures, the NRI geometry is quite

uniform and the yield is high.

1.6Research Motivations

Because of the interferometry imaging nature of OCT and the strong coherent scattering characteristics of localized surface plasmon (LSP) resonance on a metal nanoparticle (NP), OCT scanning is an effective approach for mapping the distribution of metal NP in a bio-tissue of bio-solution. In particular, by properly designing the relative spectral positions of the LSP resonance of the metal NP and the OCT light source, a metal NP distribution can be identified through the spectroscopic operation of an OCT system of a large source spectral width. In this study, we build a high-resolution OCT system to scan human oral cancer cell solutions with applied Au nanorings (NRIs). Although the resolution of OCT scanning is not high enough for identifying individual Au NRIs, the imaging of Au NRI clusters can help us in mapping their distribution on the membrane of the cells or inside the cells. Based on such an observation, the efficiencies of Au NRI adsorption and internalization by the cells can be evaluated. Also, the difference of linking antibody to the Au NRIs can be seen. With antibody linkage, the efficiencies of Au NRI adsorption and internalization by the cells become higher.

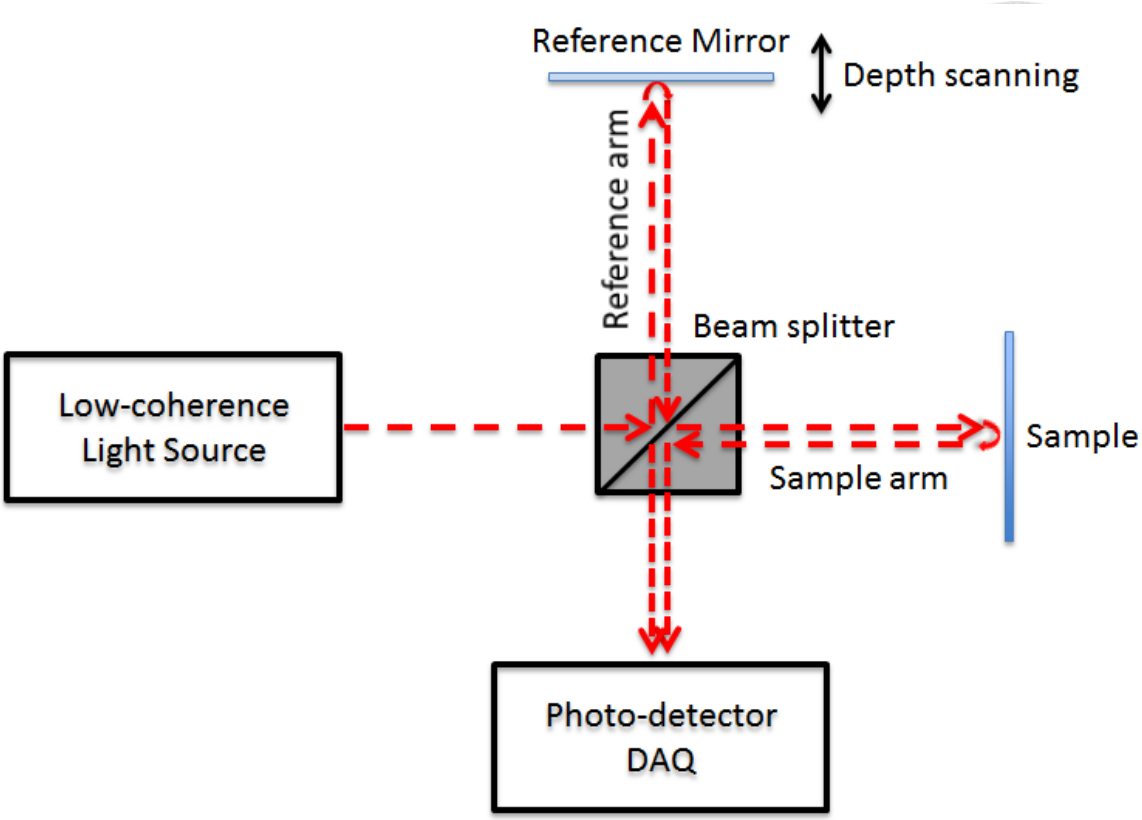

Fig. 1.1 Basic layout of an OCT system based on a Michelson interferometer.

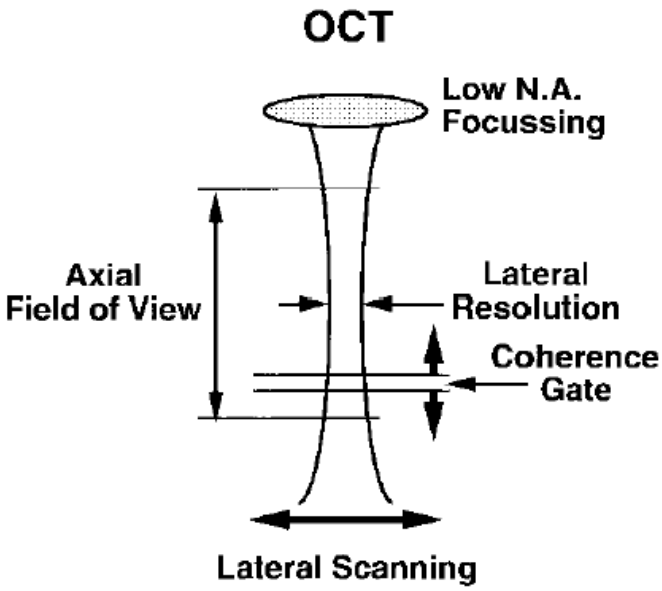

Fig. 1.2 An optical beam focused by a lens.

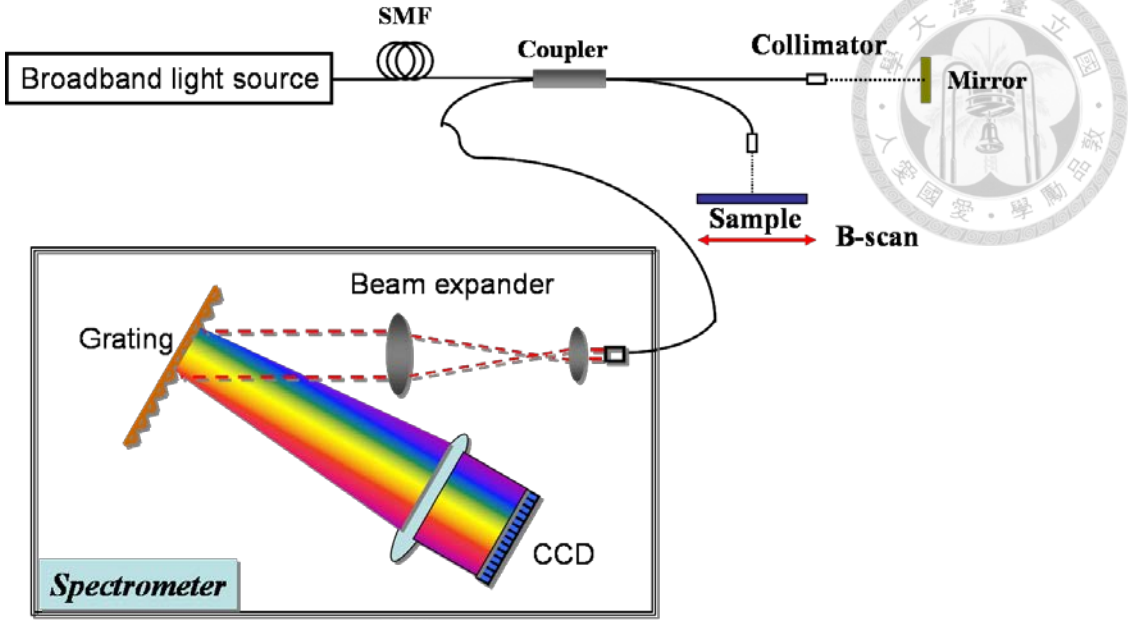

Fig. 1.3 Setup of a spectral-domain OCT system.

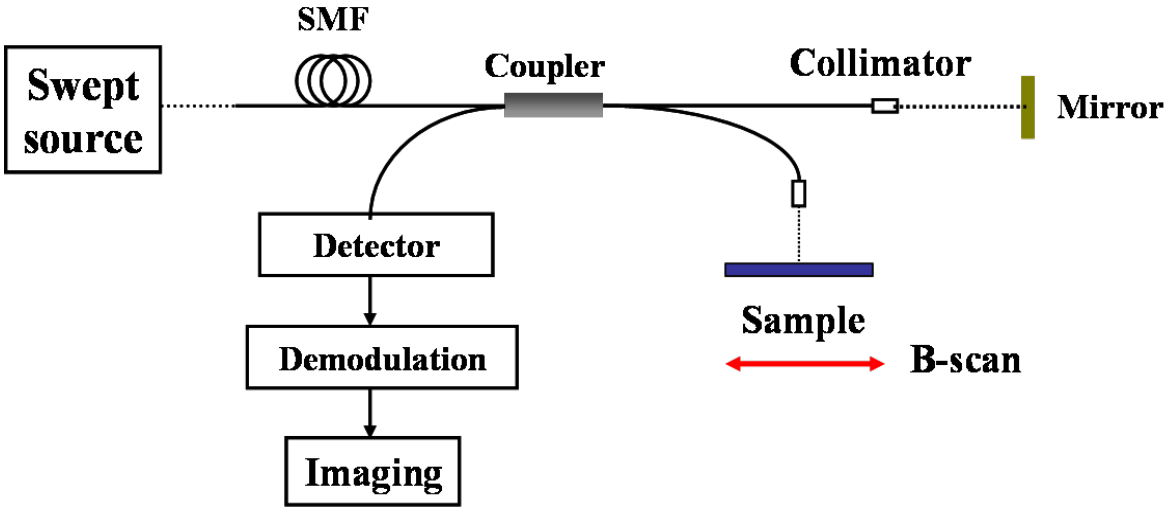

Fig.1.4 Setup of an SS-OCT system

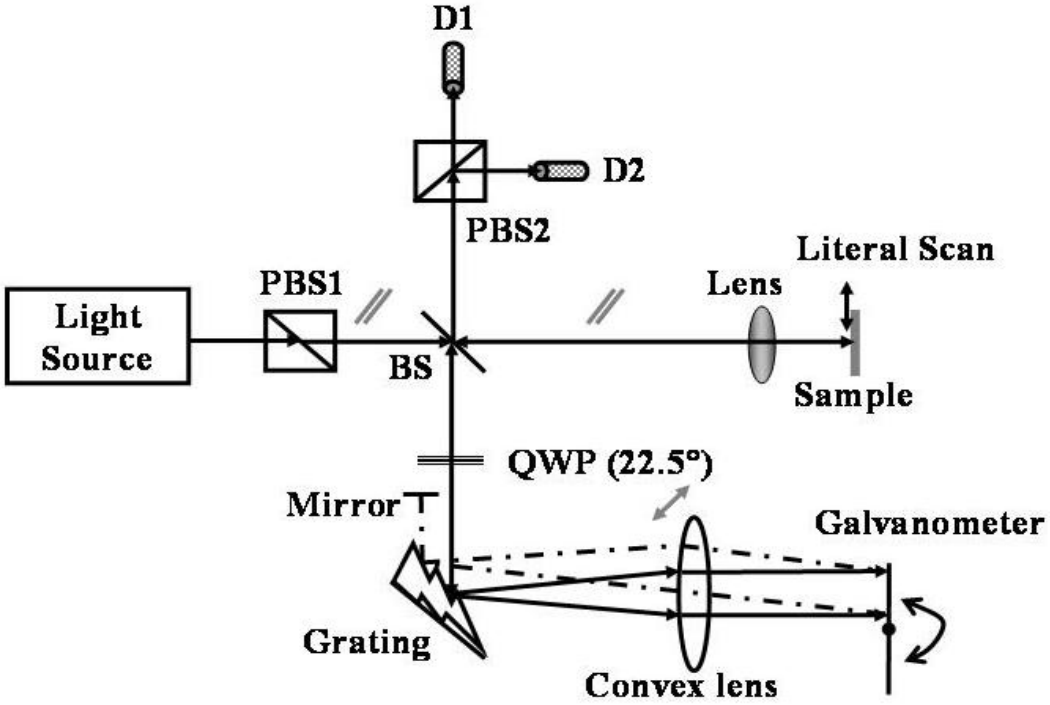

Fig. 1.5 Setup of a PSOCT system.

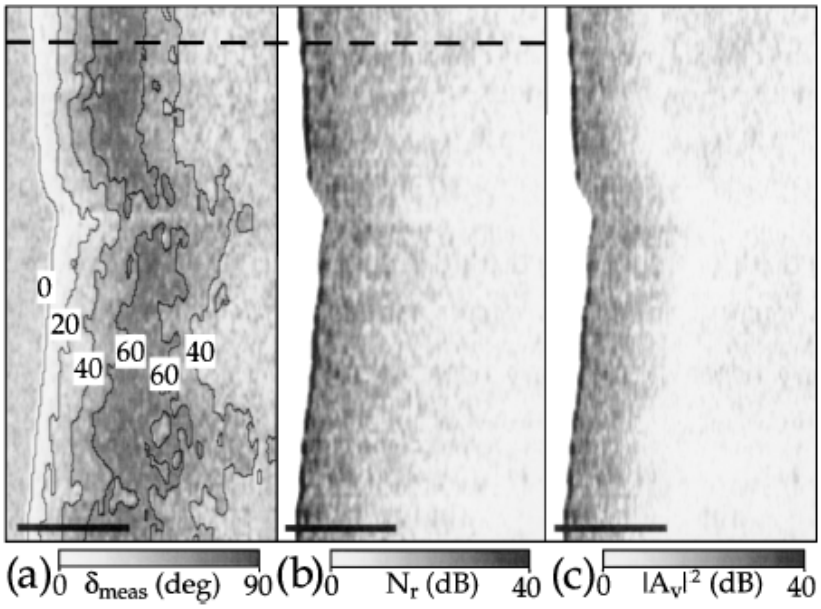

Fig. 1.6 PSOCT images. (a) Image of phase retardation caused by birefringence, (b) birefringence-independent image of tissue backscattering, (c) birefringence-dependent image of tissue generated by a single detector.

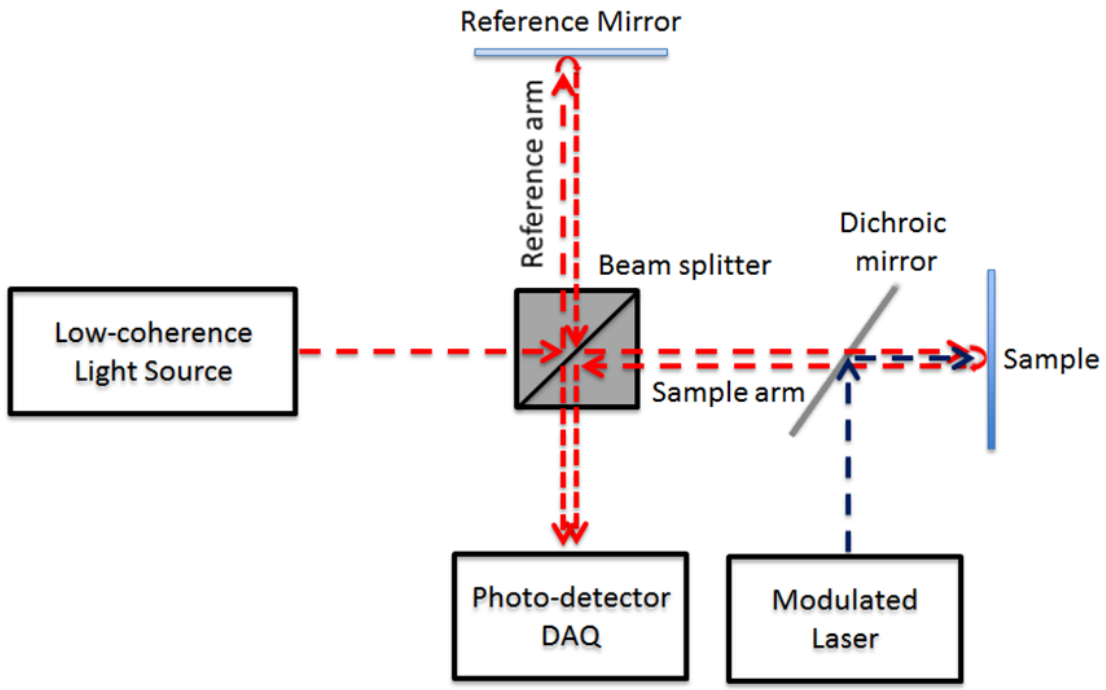

Fig. 1.7 Basic layout of a photo-thermal OCT system based on a Michelson interferometer.

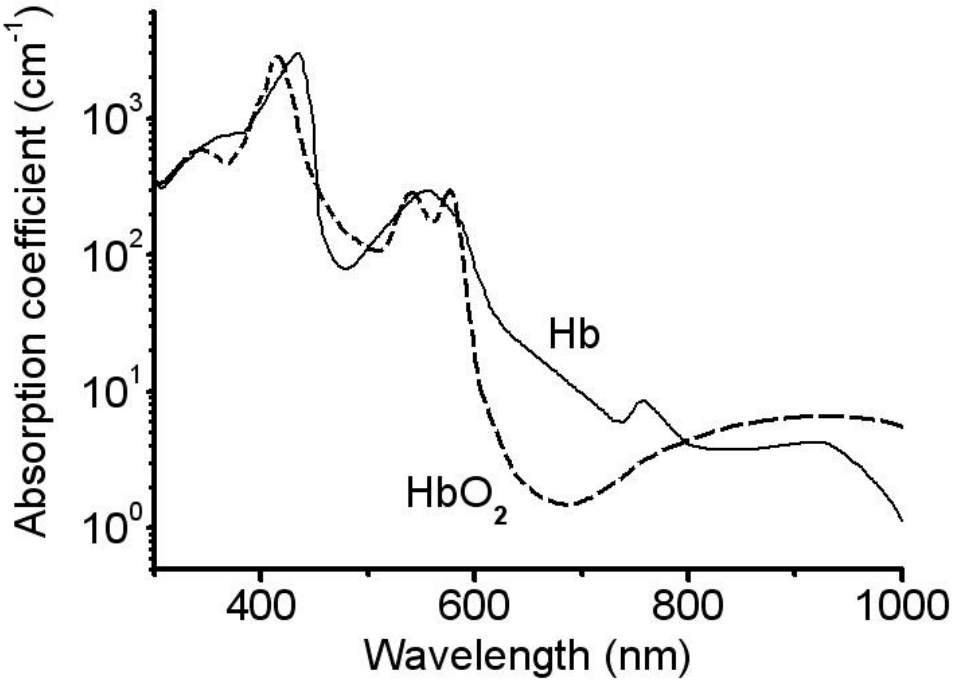

Fig.1.8 Absorption spectra of Hb and HbO_2 around 800 nm in wavelength.

Chapter 2

On-substrate Fabrication of Bio-conjugated Au Nanoring Solution

2.1 Localized Surface Plasmon

Localized surface plasmon (LSP) represents the local oscillation of free electrons on a metal nanoparticle (NP). Unlike the excitation mechanism of surface plasmonpolariton (SPP), LSP has a broad distribution of wavevector [63], such that it can be excited and can radiate in a broad range of direction. Fig.2.1 shows the dispersion relations of SPP and LSP. One can see that due to the momentum mismatch between SPP dispersion and light line, light extraction from SPP energy needs certain mechanisms to match the momentum, such as prism, grating or rough surface structures. In contrast, the dispersion relation curve of LSP crosses the light line, such that there is no need to match the momentum for the energy exchange between light and LSP. Such optical properties make LSP a good choice for the applications to light energy exchange. For example, light scattering for bio-image contrast enhancement and

light absorption for photothermal applications are widely used. LSPs can exist on rough metallic surfaces, aggregates and clusters of metal nanoparticles, as well as engineered metal nanostructures. The resonance frequency of an LSP can be tuned by controlling the size and shape of a metalnanoparticle (NP) and the refractive index of its surrounding medium. They can create strong localized electromagnetic field. At its resonance, LSP can induce enhanced scattering and absorption of a metal NP.

When an electromagnetic wave propagates through a metal NP, the energy of such an electromagnetic wave can be scattered or absorbed by the NP through LSP resonance and result in its extinction. For a homogeneous metal nanosphere, which is surrounded by an isotropic dielectric medium, as shown in Fig. 2.2, by using the quasi-static approximation, the corresponding scattering and absorption cross sections of an incident light can be written as [64] :

$$C_{Sca} \cong \frac{8\pi}{3} k^4 a^6 \left| \frac{\epsilon_1(\omega)-\epsilon_2(\omega)}{\epsilon_1(\omega)+2\epsilon_2(\omega)} \right|^2 \quad (2\text{-}1)$$

$$C_{Abs} \cong 4\pi k a^3 \mathrm{Im}\left[\frac{\epsilon_1(\omega)-\epsilon_2(\omega)}{\epsilon_1(\omega)+2\epsilon_2(\omega)} \right] \quad (2\text{-}2)$$

with$k = \frac{2\pi}{\lambda}$

Here, $\epsilon_1(\omega)$ and $\epsilon_2(\omega)$ are the complex dielectric constants of the metalnanosphere and the surrounding medium, respectively.Equations (2-1) and (2-2) show the strong dependence of the resonance frequency

on the surrounding dielectric constant. Such a strong dependence on the surrounding dielectric constant makes metal NPs the ideal choice for the refractive index sensing applications. In using the LSP resonance features in biomedical applications, Au NPs are preferred due to their biocompatibility and flexibility to conjugate biomolecules. The widely used Au NPs for biomedical applications include sphere-like solid Au NPs [65], nanorods [66-68], silica/Au nanoshells [69-71], hollow Au NPs [72, 73], and nanocages [74-76]. However, the wavelengths of the major LSP resonance modes of those Au NPs of high quality are usually shorter than 900 nm. In biomedical applications, due to weaker tissue absorption and scattering, the use of a light source with the wavelength longer than 950 nm can result in deeper tissue penetration for extending the depth ranges of diagnosis and therapy [77].Fig. 2.3 shows the relative absorption and scattering spectra of tissue, indicating clearly the deeper light penetration into tissue in the window of 950-1300 nm.Therefore, Au nanorings (NRIs) with the LSP resonance wavelengths longer than 1000 nm show their advantages of deeper-tissue biomedical application.

2.2 Surface Plasmon Resonance Characteristicsof Au Nanorings

Fig.2.4 shows the simulation results of the absorption, scattering, and

extinction (the summation of absorption and scattering) cross section spectra of an Au NRI with the outer ring radius a = 85 nm, the ring thickness d = 14.3 nm, and ring height h = 58 nm. Those NRI geometric parameters are defined in the insert of Fig. 2.4, in which a perfect NRI is schematically drawn. The simulation is undertaken by using the commercial software COMSOL. In the simulation, a plane wave is incident in the direction of 45 degrees off the dashed ring axial line for equally exciting the cross-ring and axial LSP modes. In Fig. 2.4, three peaks can be observed in each curve [78]. The long-wavelength one around 1248 nm is caused by the CRD mode of LSP. The small peak around 790 nm is generated by the cross-ring higher-order (CRH) mode of LSP. The peak around 610 nm in Fig. 2.4 corresponds to the axial dipole (AD) mode of LSP. As shown in Fig. 2.4, although the absorption cross section of an Au NRI is smaller than its scattering cross section around the CRD LSP resonance peak, the LSP-enhanced absorption of an Au NRI is still quite strong for generating the photothermal effect. The strong LSP-enhanced scattering of an Au NRI implies that it can also be a good contrast agent in optical imaging of biomedical tissue.

Fig.2.5 shows the simulation results of the peak wavelength variations of CRD LSP resonance with ring height, h, for three ring thickness values (d) when the outer ring radius, a, is fixed at 85 nm. Here, one can see that the CRD LSP resonance wavelength decreases with

increasing *d* or *h*. When *h* is sufficiently small, the CRD LSP resonance wavelength can be longer than 1200 nm. Fig.2.5 provides us with a guide for fabricating Au NRIs to make the CRD LSP resonance wavelength reach the 1300 nm range for deeper tissue penetration. Fig.2.6 shows the spectra of extinction and absorption cross sections of two NRIs with different heights. Their outer radius and ring thickness are fixed at 85 and 14.3 nm, respectively. The curves labeled by H (L) correspond to the NRI of 58 (46) nm in height. Here, one can see that as the ring height decreases and hence the CRD LSP resonance red-shifts, the absorption cross section increases even though the extinction cross section is decreased.

2.3 Fabrication of Bio-conjugated Au Nanoring

Figs.2.7(a)-2.7(g) show the fabrication procedures of bio-conjugated Au NRI solution. Figs.2.8(a)-2.8(f) show the SEM images of the on-substrate sample at different fabrication stages. In the first step, a Si nano-imprint mold is used to impress a polymer substrate for forming a nanopillar array on it. The diameter and height of the nanopillars are 180 and 100 nm, respectively. The schematic demonstration of this step and the resultant tilted SEM image of the substrate are shown in Figs. 2.7(a) and 2.8(a), respectively. Then, O_2 plasma is applied in a reactive ion etching (RIE) process to adjust the diameter and height of the nanopillars,

as shown in Figs. 2.7(b) and 2.8(b) for the schematic demonstration and the resultant SEM image, respectively. In one of the implementations leading to the results to be discussed in the following, the nanopillar diameter and height are reduced to -140 and -80 nm, respectively. Next, an Au film of ~30 nm in thickness is deposited onto the polymer substrate to serve as the source of secondary sputtering, as depicted in Fig. 2.7(c). The secondary sputtering is implemented through a process of CHF_3 RIE under the conditions of 30 SCCM in gas flow rate, 2.3 Pa in pressure, 80 W in RF power, and 635 s in RIE duration. In this process, the Au atoms on the tops of the nanopillars are removed. Meanwhile, the Au atoms on the substrate surface in the gap regions between nanopillars are sputtered onto the sidewalls of the nanopillars to form a ring shape, as depicted in Fig. 2.7(d). The tilted SEM image after this step is shown in Fig. 2.8(c). Then, another step of O_2 RIE is applied to remove the polymer inside the Au ring structure, i.e., the original pillar body. In this stage, the background substrate level is also lowered to form new pillars with the Au ring structures at the tops, as depicted in Fig. 2.7(e). The plan-view and tilted SEM images of the Au NRIs on substrate after this step are shown in Figs. 2.8(d) and 2.8(e), respectively. To enhance the robustness of the Au ring structure, the sample is thermally annealed at 170-180 ^{o}C for 10 min. The purposes of the thermal annealing process are to avoid the breakage of Au NRI after liftoff and to enhance the overall CRD LSP

resonance strength. We use the ratio of the overall LSP resonance peak level over the background level in the extinction spectrum (within the measurement range of 400-1370 nm) of an Au NRI solution at 4 as the criterion of the CRD LSP resonance strength. It is noted that RIE is a semi-physical and semi-chemical reaction process, depending on the chosen etching chemicals. With O_2 as the etching gas, RIE is essentially a chemical process and can easily etch polymers. In our operation with CHF_3, RIE mainly causes a physical process of bombarding the Au atoms to result in the effect of secondary sputtering.

Next, the bio-conjugation process is applied to the Au NRIs when they are still attached to the substrate. In this process, first, the substrate with Au NRIs is immersed in a biolinker solution for four hours to form the carboxyl groups on the surface of Au NRIs. The biolinker solution is prepared by mixing a Nanothinks acid16 (5mM in ethanol, Sigma-Aldrich) solution of 20μL with 50 mL de-ionized water. Then, the sample is rinsed in de-ionized water for several times to remove the residual biolinker. Next, the sample is immersed in a mixed solution of 30 μL (400mM) 1-ethyl-3- [3-dimethylaminopropyl] carbodiimide hydrochloride (EDC), 30μL (100mM) N-hydroxysulfosuccinimide (sulfo-NHS), and 50 mL phosphate buffer saline (PBS) solution for 20 min to activate the biolinker. Then, the monoclonal anti-EGFR

antibody(20μL, 0.5 mg/mL, Anti-EGFR (26-125) mAb, Abnova) is added to the mixed solution for antibody connection. After the interaction for 22 hours, the sample is rinsed again to remove the residual antibody and other chemicals. The bio-conjugation process is schematically depicted in Fig. 2.7(f). After this process, the tilted SEM image of the on-substrate Au NRIs is shown in Figs. 2.8(f). From the SEM images of several samples at this stage, it is estimated that ~5 % of Au NRIs can be lost during the bio-conjugation process. To transfer the Au NRIs into water solution, the substrate is placed in a glass bottle with a proper amount of de-ionized water. Sonication (NeyTech 104H with a power of 340 W for 5 min) is applied until >95 % of the NRIs, which still remain on the substrate after the bio-conjugation process, are transferred into water, as depicted in Fig. 2.7(g).Fig.2.9 shows a tilted SEM image of the substrate after Au NRI liftoff with sonication. The only Au NRI remained on the substrate is indicated by the arrow. To avoid NRI aggregation in solution, PEG-Thiol (mPEG-Thiol-5000, Laysan Bio Inc., Arab, AL) is added to the NRI solution. The concentration of PEG-Thiol in the NRI solution is 1×10^{-4} M. Fig.2.10(a) shows the SEM image of the fabricated Au NRIs when the dried-up Au NRIs are placed on a Si substrate. Fig.2.10(b) shows the photograph of Au NRI solution in a container. Its concentration is estimated to be 10^{10} per mL. The Au NRI concentration in the solution is estimated by evaluating the number of the on-substrate

Au NRIs and by assuming that 90 % of the Au NRIs are transferred into the solution.

To confirm the surface modification procedures, the zeta potential levels under different surface modification conditions of Au NRIs are measured. First, after the biolinker is applied to the Au NRIs, the zeta potential is -32.13 mV. This negative potential is due to the carboxyl groups in the biolinker. Then, after PEG-Thiol is applied to the Au NRIs besides the biolinker, the zeta potential becomes -32.25 mV, which is essentially unchanged from the condition of biolinker only. The addition of PEG-Thiol cannot significantly change the charge characteristics of the Au NRIs unless the biolinker is replaced by PEG-Thiol. The essentially unchanged zeta potential indicates that the biolinker is not replaced by PEG-Thiol. Both the biolinker and PEG-Thiol are attached to the Au NRIs. Next, when the biolinker, antibody, and PEG-Thiol are applied to the Au NRIs, the zeta potential becomes -16.78 mV. The zeta potential magnitude is reduced because the carboxyl groups of part of the biolinker are linked to the amine groups of the antibody such that the negative surface charge of the Au NRIs is decreased. Although the antibody can be directly linked to an Au NP without using a biolinker [79], we use the biolinker in this work for connecting the antibody and the Au NRIs to assure the strong bonding between them. Our zeta potential measurements confirm that the function of the biolinker works.

As shown in Fig. 2.5, a smaller ring height leads to a longer CRD LSP resonance wavelength. To push this wavelength closer to 1300 nm, another CHF_3 RIE process can be applied after the step of Fig. 2.7(d) for adjusting the ring height. With the second CHF_3 RIE process, the Au atoms attached to the sidewall of a polymer nanorod can be removed from the top to make the fabricated Au NRI shorter (smaller *h*), as schematically shown in Fig. 2.11(a).Figs.2.11(b)-2.11(f) show the tilted SEM images of NRI arrays on polymer substrate after the fabrication stage shown in Fig. 2.7(e) is finished with the second CHF_3 RIE durations at 0, 70, 150, 190, and 250 sec (assigned as samples I-V, respectively) under the conditions of 30 SCCM in gas flow rate, 2.3 Pa in pressure, and 100 W in RF power. One can see that the NRI height decreases with increasing duration of the second CHF_3 RIE process. In the insert at the lower-right corner of each of Figs. 2.11(b)-2.11(f), the SEM image of an individual NRI after liftoff is shown. The NRI heights of samples I-V are estimated to be 78, 67, 58, 49, and 37 nm, respectively. Their ring diameters and thicknesses are individually about the same. The normalized extinction spectra of those samples (solutions) are shown in Fig. 2.12. Here, one can see that the resonance wavelengths of both CRD and CRH LSP modes red-shift with decreasing ring height. However, the resonance wavelength of the AD LSP mode blue-shifts with decreasing ring height. The CRD LSP resonance peak wavelengths of samples I-V

are 1130, 1187, 1248, 1285, and 1305 nm, respectively. It is noted that the ratio of the CRD LSP resonance strength over that of the AD LSP mode in experiment is larger than the ratio obtained from the simulation shown in Fig. 2.4 (equal excitation of the two LSP modes). This comparison result can be explained by the observation that the fabricated Au NRIs are non-uniform along the ring axis such that the AD LSP resonance becomes weaker. It is noted that smaller NRIs can be produced by further reducing the polymer pillar size in the first O_2 RIE step. Fig.2.13(a) shows the SEM images of various stages in reducing the pillar size. One can see that the size of the polymer pillars can be reduced to ~50 nm. Figs.2.13(b)-2.13(d) show the SEM images of the fabricated small Au NRIs with outer diameters at ~105 nm (Figs. 2.13(b) and 2.13(c)) and ~95 nm (Fig. 2.13(d)). The extinction spectra of those small NRIs are shown in Fig. 2.13(e). One can see that the extinction peaks of the NRIs of 105 and 95 nm in size are at 1015 and 950 nm in water, respectively.

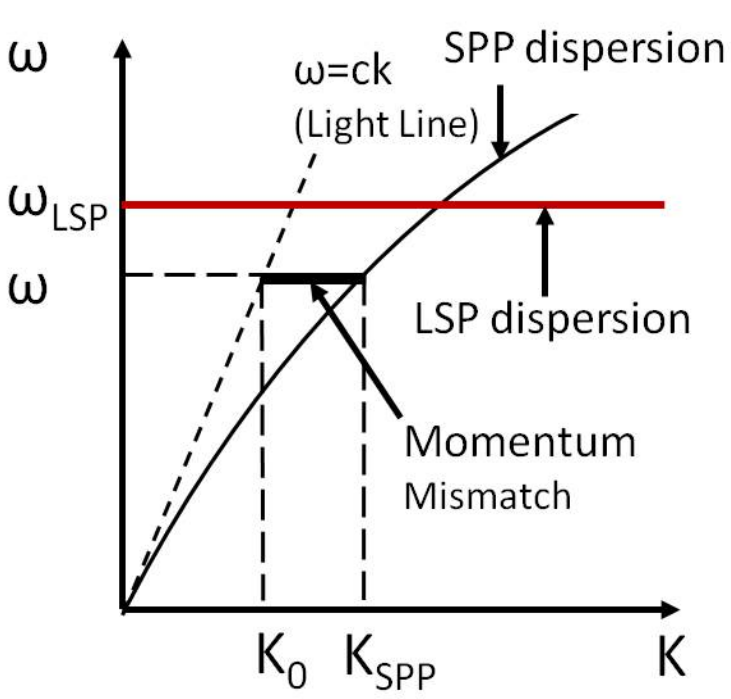

Fig. 2.1 Dispersion relation of SPP and LSP. Due to the momentum mismatch between SPP dispersion and light line, light extraction from SPP energy needs certain mechanisms to match the momentum, such as prism, grating or rough surface structures. In contrast, there is no need to match the momentum for the energy exchange between light and LSP.

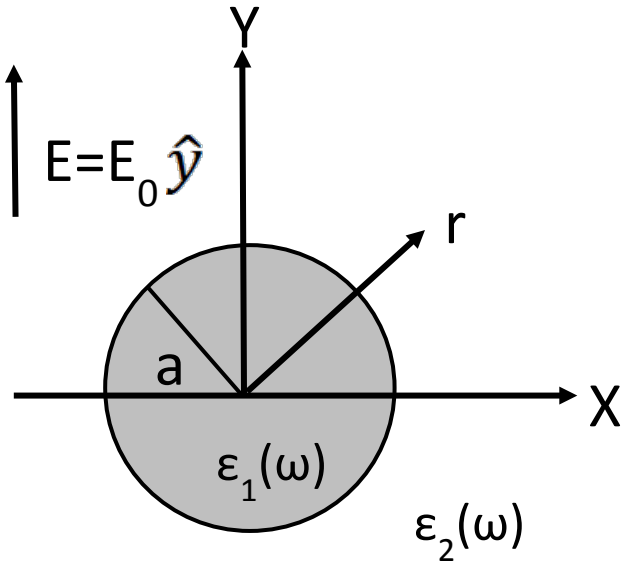

Fig. 2.2 Sketch of a homogeneous metallic sphere surrounded by an isotropic dielectric medium in a uniform static electric field.

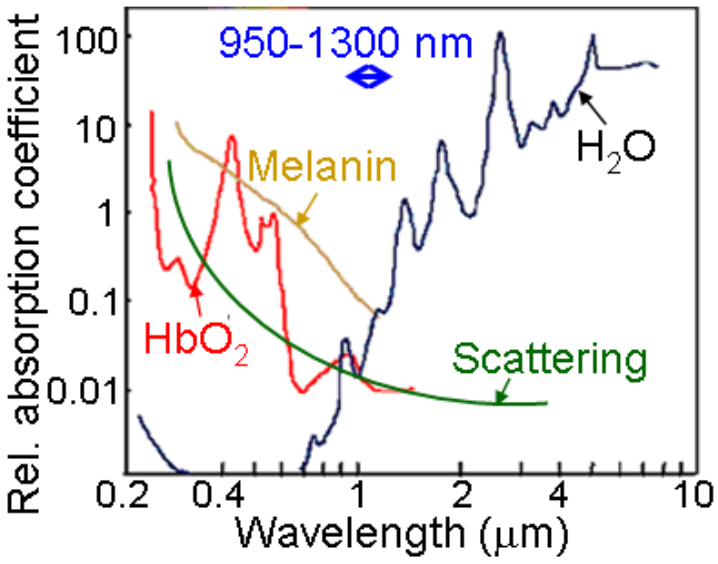

Fig. 2.3 Relative absorption and scattering spectra of tissue.

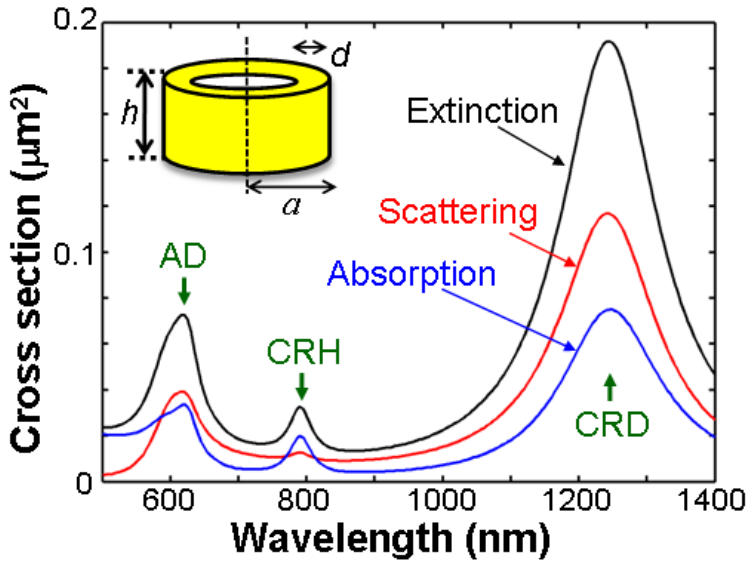

Fig.2.4Simulation results of the absorption, scattering, and extinction cross section spectra of a typical Au NRI with the outer ring radius a = 85 nm, the ring thickness d = 14.3 nm, and ring height h = 58 nm. The NRI parameters are defined in the insert.

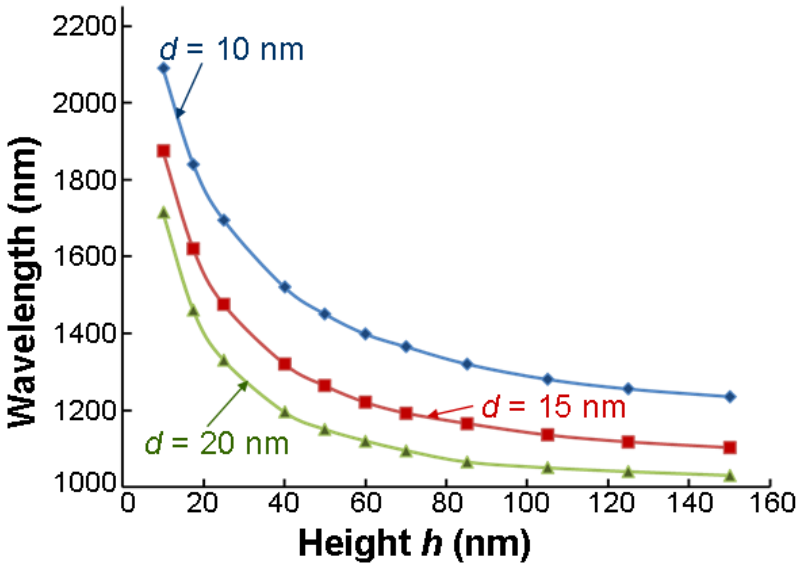

Fig.2.5 Simulation results of the resonance wavelength variations of the CRD LSP mode with ring height, h, for three ring thickness values when the outer ring radius is fixed at 85 nm.

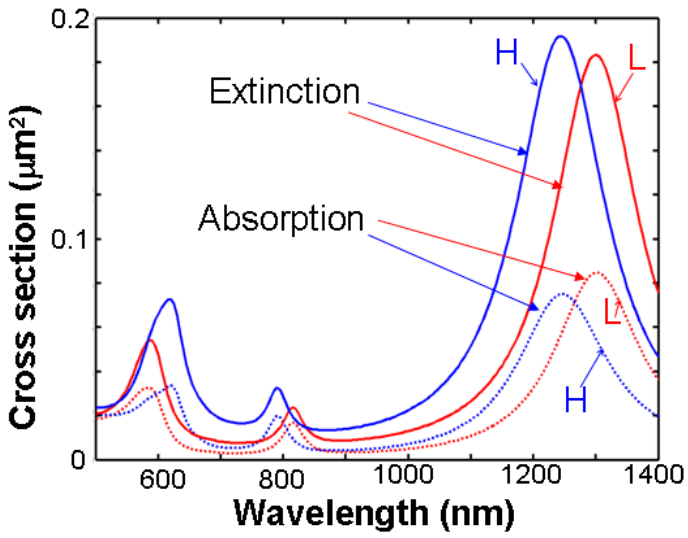

Fig.2.6 Spectra of the extinction and absorption cross sections of two NRIs with different heights at h = 58 nm (labeled by H) and h = 46 nm (labeled by L). The outer ring radius and thickness are fixed at 85 and 14.3 nm, respectively.

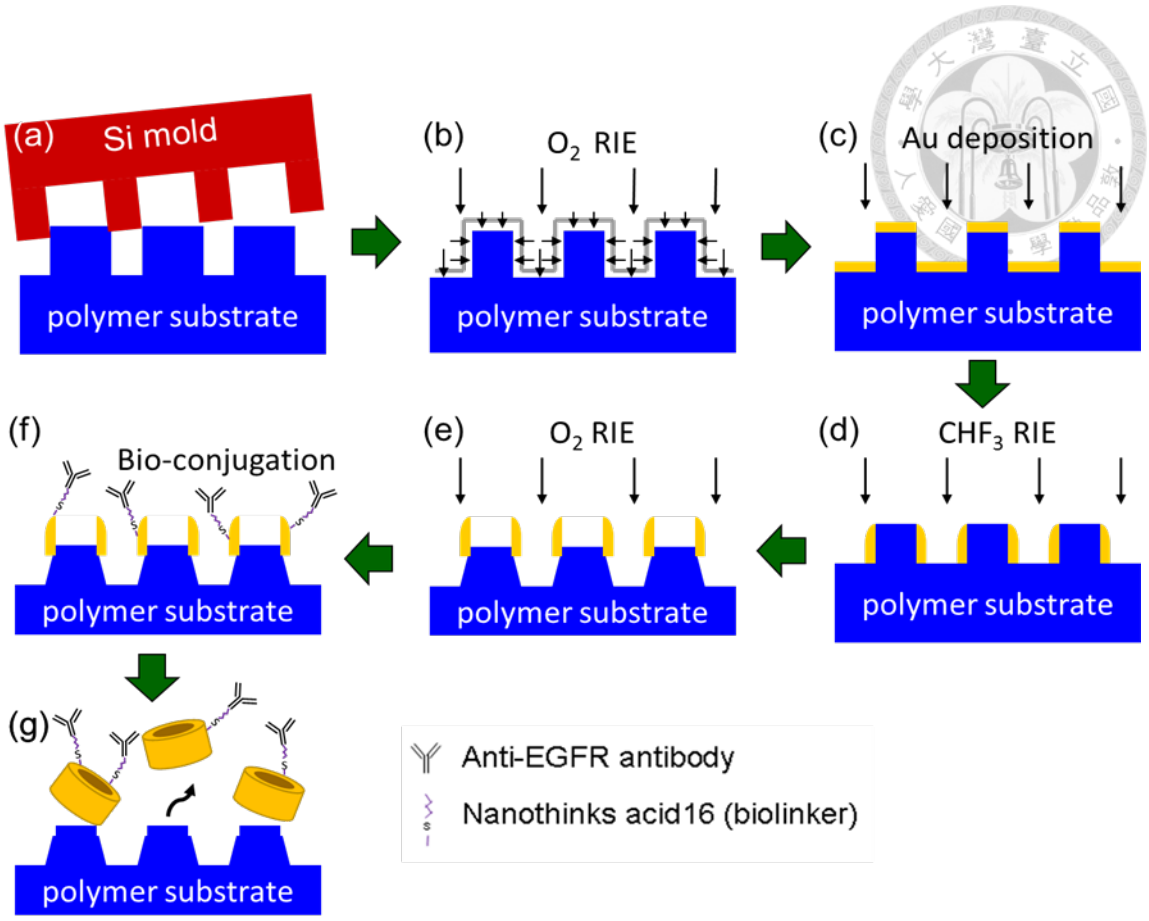

Fig.2.7 Fabrication procedures of bio-conjugated Au NRI solution. (a): Nano-imprint step to prepare the polymer substrate with nanorods; (b): First O_2 RIE step to modify the geometry of the polymer nanorods; (c): Au deposition step. (d): CHF_3 RIE step for secondary sputtering of Au to form the ring shape. (e): Second O_2 RIE step to remove the polymer nanorods and lower the substrate surface. (f): Bio-conjugation step. (g): Sonication step to transfer Au NRIs into water solution.

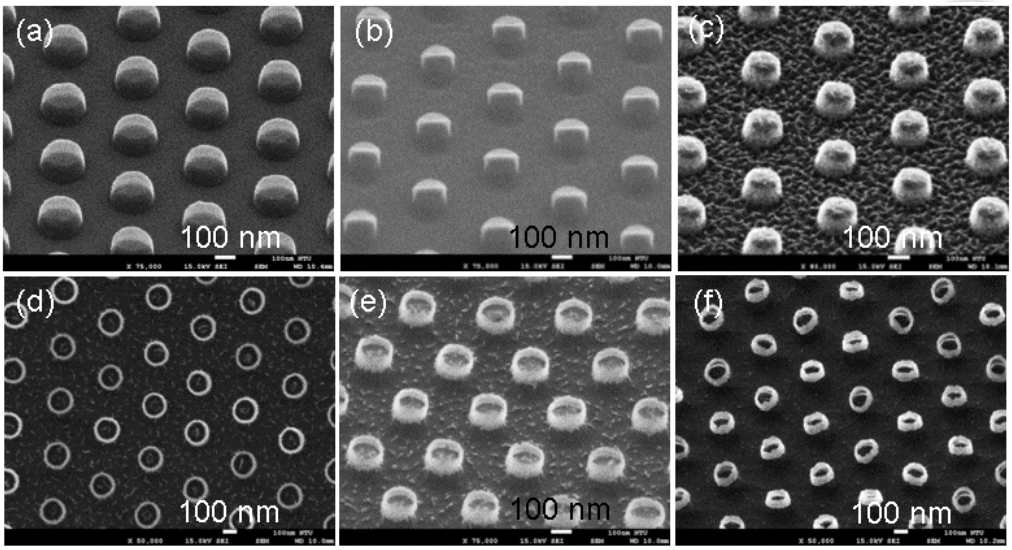

Fig.2.8 SEM images on the substrate showing the results after various fabrication steps. (a): After the nano-imprint step. (b): After the first O2 RIE step. (c): After the Au deposition and CHF3 RIE steps; (d) and (e): After the second O2 RIE step (plan-view and tilted-view, respectively). (f): After the bio-conjugation process.

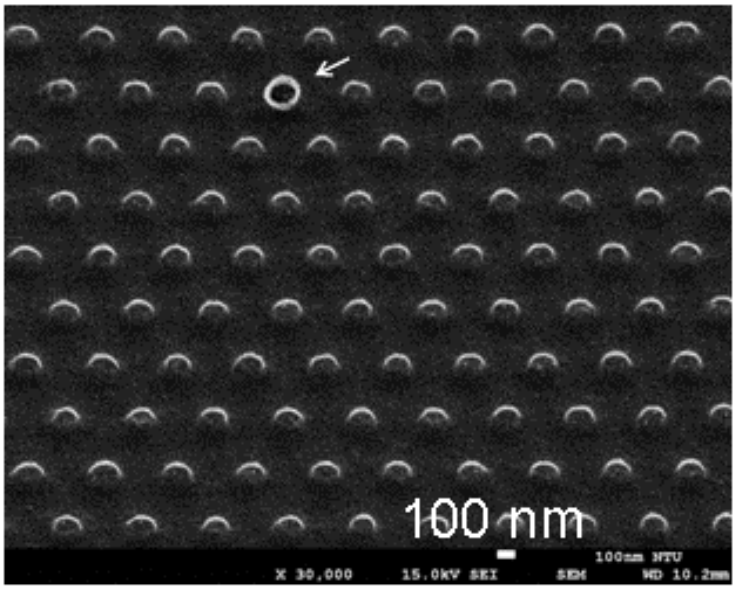

Fig.2.9 Tilted SEM image of the substrate after Au NRI liftoff with sonication. The Au NRI remained on the substrate is indicated by the arrow.

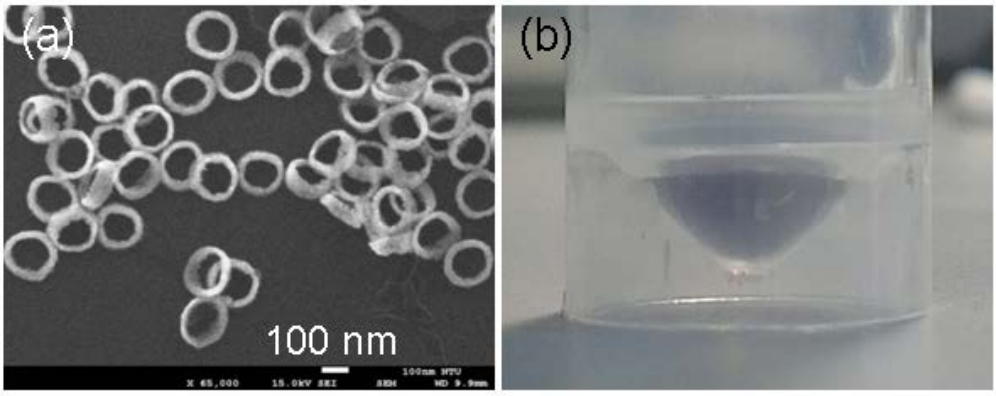

Fig.2.10 (a): SEM image of the fabricated Au NRIs taken when the dried-up Au NRIs are placed on a Si substrate. (b): Photograph of an Au NRI solution in a container.

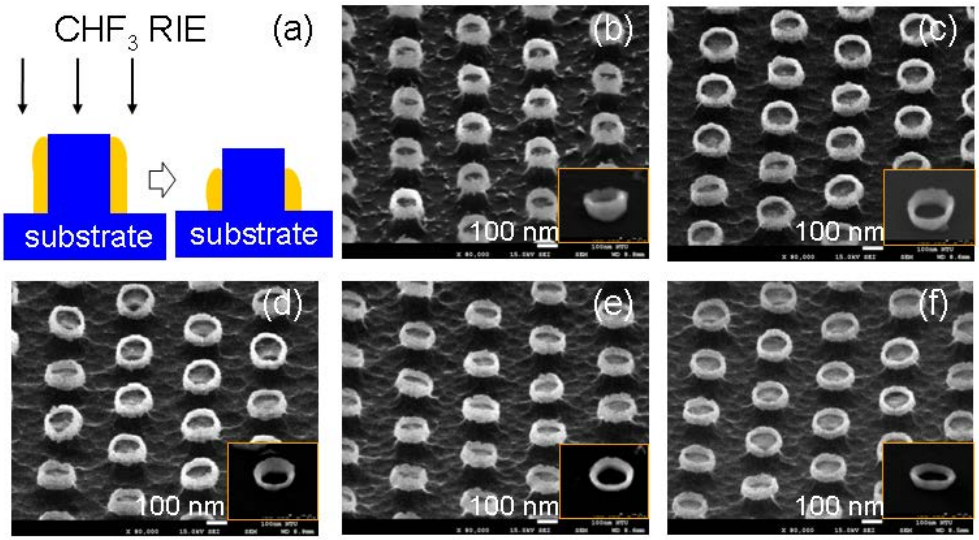

Fig.2.11 (a): Schematic drawing to show the reduction of ring height in the second CHF_3 RIE process. (b)-(f): Tilted SEM images of NRI arrays on polymer substrate (samples I-V, respectively) after the second CHF_3 RIE processes of different durations. In the insert at the lower-right corner of each of parts (b)-(f), the SEM image of an individual NRI after liftoff is shown.

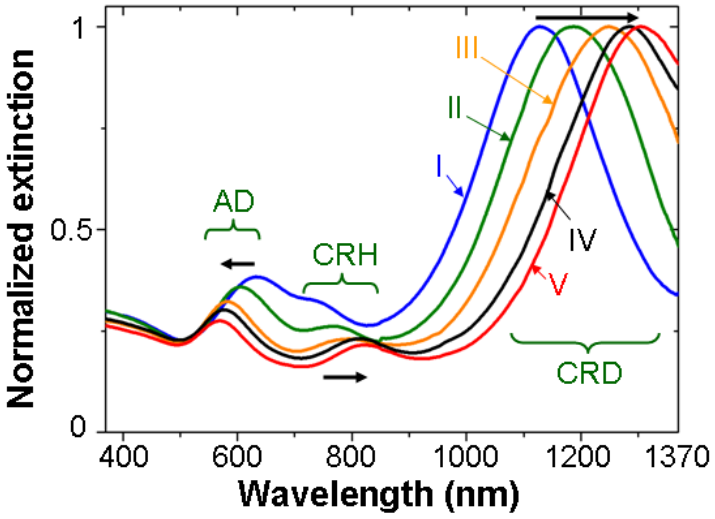

Fig.2.12 Normalized extinction spectra of NRI solutions corresponding to samples I-V shown in Figs. 2.8(b)-2.8(f).

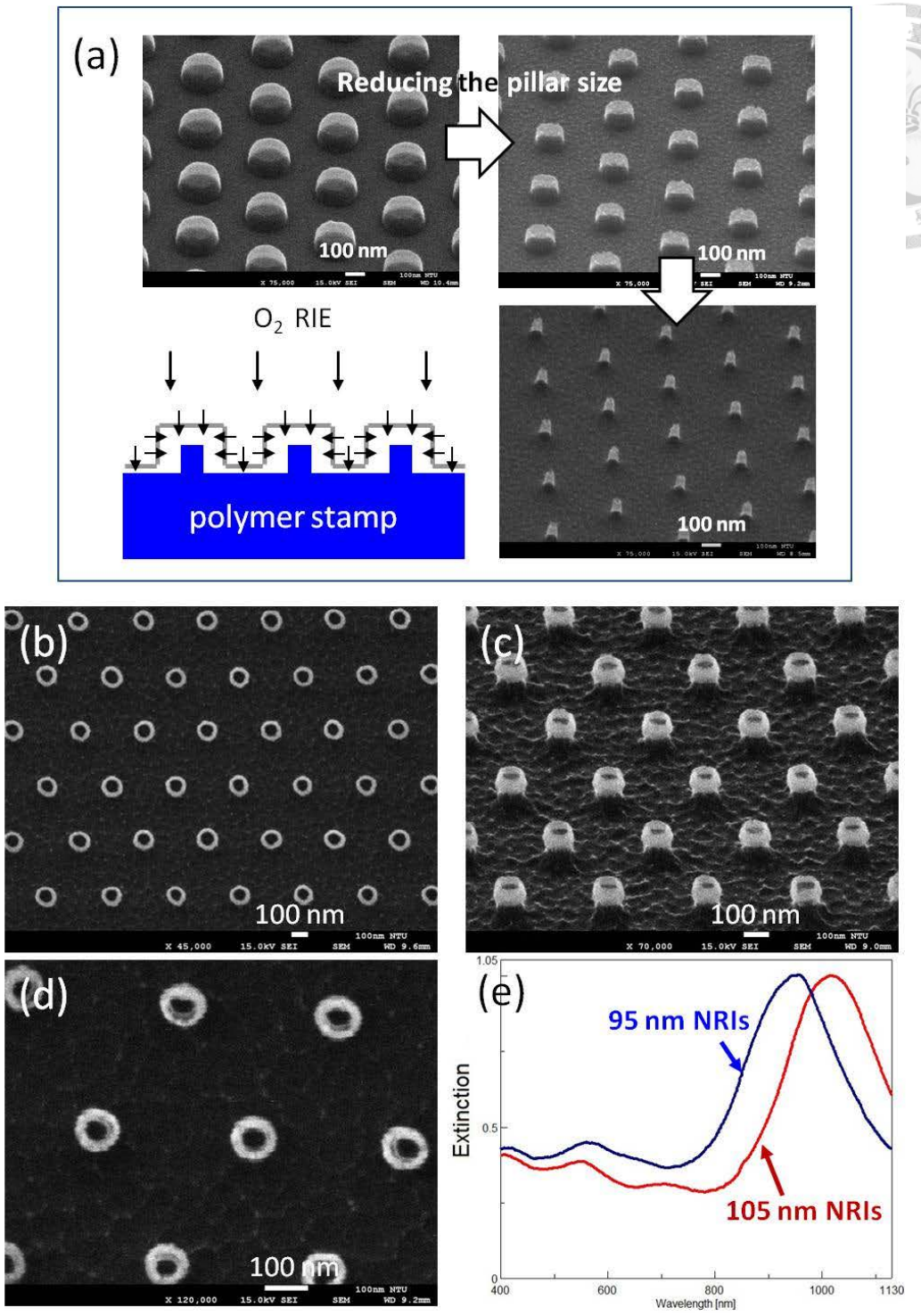

Fig.2.13 (a) SEM images of various stages in reducing the polymer pillar size. (b)-(d): SEM images of the fabricated small Au NRIs with outer diameters at ~105 (parts (b) and (c)) and ~95 nm (part (d)). (e) Extinction spectra of the small NRIs.

Chapter 3

Optical Coherence Tomography Scanning Results and Discussions

3.1 Experimental Setup and Sample Preparation

Fig.3.1 shows the setup of the used OCT system. Here, a super-luminescent diode with its output spectrum shown in the red curve of Fig. 3.2 is used as the light source of the free-space OCT system. In the sample arm of the Michelson interferometer, a two-dimensional (2-D) scanning galvanometer is used for scanning the cell sample from the bottom of a cultured well to form a 3-D image. In the detection arm, a spectrometer, including a beam expander, a diffraction grating, a lens, and a 1-D CCD, is built for collecting the interfered spectrum of OCT scanning data. As shown in Fig. 3.2, the multiple-hump source spectrum covers a full-width at half-maximum of around 200 nm (from ~760 nm through ~960 nm). The depth resolution is ~2 microns in air. In the sample arm, a 40X objective lens is used for focusing OCT light onto the sample. The lateral resolution in OCT scanning is <4 microns. The sensitivity of the OCT system is ~100 dB. A 3-D image includes 300, 500, and 500 pixels in the A-, B-, and C-modes, respectively. The 3-D

scanning time is 10 sec. The pink dashed line marked at 860 nm in Fig. 3.2 divides the OCT source spectrum into the long- and short-wavelength portions for spectroscopic imaging processing.

The insert of Fig. 3.2 shows the scanning electron microscopy (SEM) image of the used Au NRIs before liftoff (still on the substrate). The black curve in Fig. 3.2 shows the normalized LSP extinction spectrum. The major peak at ~980 nm, marked by the arrow, corresponds to the cross-ring LSP dipole resonance mode. The secondary peak at ~700 nm originates from the mixture of the cross-ring high-order LSP resonance and the axial resonance modes. One can see that the long-wavelength portion of the OCT source spectrum overlaps an LSP extinction spectral range of significantly stronger LSP resonance, when compared with that of the short-wavelength portion of the OCT source spectrum. Therefore, when OCT signal is scattered by Au NRIs, the signal intensity in the long-wavelength portion is stronger than that in the short-wavelength portion. From such a spectroscopic analysis, we can better identify the distribution of Au NRIs. Fig.3.3 shows the four steps of cancer cell scanning with the OCT system. Two kinds of human oral cancer cells, including SCC4 and SAS, are used for experiment. The cell well is scanned from the bottom as shown in each part of Fig. 3. Also, both cases of linking antibody and without antibody are considered for OCT scanning. As shown in Fig. 3(a), the cell solution is scanned before the

application of Au NRIs for identifying a couple cells, which are settled at the bottom of the well. The OCT scanning will be focused at these cells for observing their NRI adsorption and internalization processing after Au NRIs are applied to the cell solution. Then, as shown in Fig. 3(b), these cells are again scanned once every hour after the application of Au NRIs to the cell well (the condition of pre-washout). After a certain number of hours for incubation, the Au NRIs either not adsorbed or internalized are washed. After washout (the condition of post-washout, see Fig. 3(c)), the target cells are then scanned again. Finally, the adsorbed Au NRIs on cell membranes are etched with KI/I2 solution and washed gain (the condition of after-etching, see Fig. 3.3(d)). The targeted cells are scanned again under this condition. Figs.3.4(a)-(c) show the OCT scanning images of Au NRI solution under the image processing conditions of full spectrum, long-wavelength portion, and short-wavelength portion, respectively. The Au NRI concentration is about $1.3\times10^{10}cm^{-3}$. Here, one can see that the OCT signal intensity in the long-wavelength image is significantly stronger than that in the short-wavelength image, indicating the effective function of spectroscopic OCT operation. Because of the smaller spectral widths in Figs. 3.4(b) and 3.4(c), their depth resolutions become poorer.

3.2 OCT Scanning Results of SCC4 Cancer Cells

Figs.3.5(a) and 3.5(b) show the 3-D OCT images of a few SCC4 cells before the application of Au NRIs. Antibody is not linked to the Au NRIs in this part of experiment. Figs.3.6(a) and 3.6(b) show the 3-D OCT images of the same SCC4 cells 24 hours after the application of Au NRIs. Here, one can see that the cells are covered by the settled Au NRIs. Then, Figs. 3.7(a) and 3.7(b) show the 3-D OCT images of the same SCC4 cells after washout. In this situation, only the adsorbed or internalized Au NRIs are preserved in the cell solution. From Figs. 3.5-3.7, we can see that the details of the cell structure cannot be clearly observed in the 3-D images.

Figs.3.8(a) -3.8(c) show the B-mode OCT scanning images of an SCC4 cell under the image processing conditions of full spectrum, long-wavelength portion, and short-wavelength portion, respectively, before Au NRI application. The bright stripes in the images correspond to the bottom of the container. As shown in Fig. 3.8(a), the nucleus and the surrounding membrane of the SCC4 cell can be clearly seen. In Figs. 3.8(b) and 3.8(c), although only one-half source spectrum is used for image processing such that the depth resolution is degraded, the nucleus and membrane can still be seen. It is noted that for making reasonable comparisons between the long- and short-wavelength images, the signal intensity of the short-wavelength image is enhanced by a factor of 3.15 to

make the images in Figs. 3.8(b) and 3.8(c) as similar as possible, as to be further explained in the discussion section. This intensity enhancement for the short-wavelength image of cancer cells will be applied to all the images below in the same experiment.

Figs.3.9(a) -3.9(c) show the B-mode OCT scanning images of the SCC4 cell, same as that in Figs. 3.8(a) -3.8(c), under the image processing conditions of full spectrum, long-wavelength portion, and short-wavelength portion, respectively, 6 hours after the Au NRIs (without linking the antibody) are added to the cell solution. Here, the bright spots outside the cell correspond to suspended Au NRIs in the cell solution. Although certain Au NRIs are adsorbed onto the membrane of the cell, in this cross section of the cell, few internalized Au NRI can be observed at this stage. By comparing Figs. 3.9(b) and 3.9(c), one can see that although Au NRIs can still be observed in the short-wavelength image, their signal intensity is weaker. It is noted that the bright spots outside the cell can also be caused by the debris of dead cells. Figs.3.10(a) -3.10(c) show the B-mode OCT scanning images of the SCC4 cell under the image processing conditions of full spectrum, long-wavelength portion, and short-wavelength portion, respectively, 12 hours after the Au NRIs are added to the cell solution. Here, we can see more Au NRIs are settled at the bottom of the container. Also, certain weak bright spots can be seen inside the cell besides the signal from the nucleus, indicating that

more and more Au NRIs are internalized. Figs.3.11(a)-3.11(c) show the B-mode OCT scanning images of the SCC4 cell under the image processing conditions of full spectrum, long-wavelength portion, and short-wavelength portion, respectively, 24 hours after the Au NRIs are added to the cell solution. Here, we can see that certain Au NRIs are internalized to show more bright spots inside the cell, particularly at the image location left to the nucleus, as indicated by the red-dashed circle. Figs.3.12(a)-3.1(c) show the B-mode OCT scanning images of the SCC4 cell under the image processing conditions of full spectrum, long-wavelength portion, and short-wavelength portion, respectively, after the washout of Au NRIs. Here, one can see that all the suspended and settled Au NRIs are removed. By comparing Figs. 3.12(b) with 3.12(c), we can see that some bright spots (including some dim spots), either on the cell membrane or inside the cell, in Fig. 3.12(b) become unclear in Fig. 3.12(c). Those bright spots are attributed to the adsorbed or internalized Au NRIs.

Figs.3.13(a)-3.13(c) show the en-face OCT scanning images of a SCC4 cell under the image processing conditions of full spectrum, long-wavelength portion, and short-wavelength portion, respectively, before Au NRI application. These en-face images clearly show the position of the nucleus. The image intensity in Fig. 3.13(c) is adjusted to make it similar to Fig. 3.13(b). It is noted that the image resolutions in

Figs. 3.13(b) and 3.13(c) are the same as that in Fig. 3.13(a) because the use of one-half spectrum in image processing does not affect the lateral resolution of the OCT system. Figs.3.13(d)-3.13(f) show the en-face OCT images, similar to those in Figs. 3.13(a)-3.13(c), respectively, 2 hours after Au NRI application. With the signals of the suspended Au NRIs outside the cells, the cross-sectional shape of the cell at the upper-left corner can be more clearly seen. At this stage, Au NRIs adsorbed onto the cell membrane can be seen. 3.13(g)-3.13(i) show the en-face OCT images, similar to those in Figs. 3.13(d)-3.13(f), respectively, 10 hours after Au NRI application. Here, we can see that more Au NRIs are settled to the depth level of the en-face image. The bright image spots circled by the red dashed line in Fig. 3.13(e) are not seen in Fig. 3.13(f), indicating that they originate from either the adsorbed or internalized Au NRIs.

Figs.3.14(a)-3.14(c) (3.14(d)-3.14(f) and 3.14(g)-3.14(i)) show the en-face OCT images, similar to those in Figs. 3.13(g)-3.13(i), respectively, 11 (12 and 13, respectively) hours after Au NRI application. The circled areas in these Figs. show the differences between the long- and short-wavelength images, which are attributed to the adsorbed and internalized Au NRIs. Figs.3.15(a)-3.15(c) (3.15(d)-3.15(f) and 3.15(g)-3.15(i)) show the en-face OCT images, similar to those in Figs. 3.14(g)-3.14(i), respectively, 16 (17 and 23, respectively) hours after Au NRI application. Again, the circled areas in these Figs. show the

differences between the long- and short-wavelength images, which are attributed to the adsorbed and internalized Au NRIs. Figs.3.16(a)-3.16(c) show the en-face OCT images, similar to those in Figs. 3.15(g)-3.15(i), respectively, 24 hours after Au NRI application. On the other hand, Figs.3.16(d)-3.16(f) show the en-face OCT images, similar to those in Figs. 3.16(a)-3.16(c), respectively, after washout. Here, we can see that after washout, the Au NRIs not adsorbed or internalized are removed to give a clear background. By comparing Fig. 3.16(a) with 3.13(a), we can see that although the morphology of the target cell and the neighboring ones after Au NRI application and washout is slightly changed from that before Au NRI application, the relatively stronger signal intensity at the cell membrane due to Au NRI adsorption can be clearly seen. Also, the dim spots circled by red dashed line, which cannot be seen in Fig. 3.13(a), clearly indicate the internalized Au NRIs.

We also use the Au NRIs with antibody for the similar experiment. Unfortunately, because the cultured SCC4 cells may not be so healthy such that the cell size is smaller and the OCT image is not so clear. However, we can still observe the processing of cell uptake. In particular, we include the condition of the KI/I2 etching of the adsorbed Au NRIs for OCT scanning. Figs.3.17(a)-3.17(c) show the B-mode OCT scanning images of two or more SCC4 cells under the image processing conditions of full spectrum, long-wavelength portion, and short-wavelength portion,

respectively, before Au NRI application. Then, Figs. 3.17(d)-3.17(f) show the B-mode OCT scanning images, similar to those in Figs. 3.17(a)-3.17(c), respectively, 24 hours after Au NRI application. Figs.3.18(a)-3.18(c) and 3.18(d)-3.18(f) show the similar B-mode OCT images after washout and after etching, respectively. In Figs. 3.18(a)-3.18(c), the signals on the container at the bottom can be due to the incomplete washout. Those signals are removed after the etching processing. The strong OCT signals at the locations of cells indicate the strong internalization of Au NRIs into the cell. The stronger Au NRI adsorption and internalization in this experiment are attributed to the antibody linkage of the Au NRIs.

3.3 OCT Scanning Results of SAS Cancer Cells

Figs.3.19(a) and 3.19(b) show the 3-D OCT images of one or two SAS cells before the application of Au NRIs. Antibody is linked to the Au NRIs in this part of experiment. Figs.3.20(a) and 3.20(b) show the 3-D OCT images of the same SAS cells 24 hours after the application of Au NRIs. Here, again, one can see that the cells are covered by the settled Au NRIs. Then, Figs. 3.21(a) and 3.21(b) (3.22(a) and 3.22(b)) show the 3-D OCT images of the same SAS cells after washout and after etching, respectively. Here, one can see that the SAS cell size is smaller, when compared with SCC4.

Figs.3.23(a) -3.23(c) show the en-face OCT scanning images of two attached SAS cells under the image processing conditions of full spectrum, long-wavelength portion, and short-wavelength portion, respectively, before Au NRI application. Here, one can see that the cell sizes are indeed smaller such that the image of the nucleus is unclear. It is noted that for making reasonable comparisons between the long- and short-wavelength images, the signal intensity of the short-wavelength image is enhanced by a factor of 1.82 to make the images in Figs. 3.23(b) and 3.23(c) as similar as possible, as to be further explained later in the discussion section. This intensity enhancement for the short-wavelength image of cancer cells will be applied to all the images below in the same experiment. Figs.3.23(d) -3.23(f) (3.23(g) -3.23(i)) show the en-face OCT images, similar to those in Figs. 3.23(a) -3.23(c), respectively, 3(15) hours after Au NRI application. From 3 to 15 hours after Au NRI application, the cell distribution and morphology seem to have been changed. The partly dark areas in Figs. 3.23(g) -3.23(i) may cover a few attached cells. The circled regions in Figs. 3.23(h) and 3.23(i) show the differences between the long- and short-wavelength OCT images, indicating that they may correspond to adsorbed or internalized Au NRIs. Figs.3.24(a)-3.24(c),3.24(d)-3.24(f), and 3.24(g) -3.24(i) show the en-face OCT images of the same lateral region at different depths under the image processing conditions of full spectrum, long-wavelength

portion, and short-wavelength portion, respectively, 24 hours after Au NRI application. The images in the second (third) row correspond to the depth 7 microns deeper than those in the first (second) row. Here, the black holes in Figs. 3.24(d)-3.24(i) may be caused by an air bubble in the cell solution because of the heating by the OCT light. Because the images here are taken at the depths above the bottom of the container, the images of most settled Au NRIs are not seen here such that the backgrounds of the images here are not so bright. The bright regions in these Figs. correspond to the cell distribution with adsorbed and internalized Au NRIs.

Figs.3.25(a)-3.25(i) show the en-face OCT images corresponding to those in Figs. 3.24(a)-3.24(i), respectively, after washout. Here, the bright backgrounds disappear because the Au NRIs not adsorbed or internalized are removed. The bright regions here correspond to either adsorbed or internalized Au NRIs. Because of the stronger scattering of Au NRIs in OCT imaging, when compared with cell structure, the OCT signals here mainly originate from Au NRI distribution. Figs.3.26(a)-3.26(i) show the en-face OCT images corresponding to those in Figs. 3.25(a)-3.25(i), respectively, after etching. Here, all the bright regions are supposed to correspond to the internalized Au NRIs. However, it is now difficult to differentiate one cell from another in the OCT images because the scanning resolution is not high enough. Nevertheless, we can still observe

the high Au NRI uptake efficiency of the SAS cells when the antibody is linked to the Au NRIs.

Figs.3.27(a)-3.27(c) show the B-mode OCT scanning images of one or more SAS cells under the image processing conditions of full spectrum, long-wavelength portion, and short-wavelength portion, respectively, before Au NRI application. Then, Figs. 3.27(d)-3.27(f) show the B-mode OCT scanning images, similar to those in Figs. 3.27(a)-3.27(c), respectively, 24 hours after Au NRI application. Figs.3.28(a)-3.28(c) and 3.28(d) -3.28(f) show the similar B-mode OCT images after washout and after etching, respectively. Again, with antibody linkage, the cell uptake efficiency of Au NRI is quite high.

3.4 Discussions

Figs.3.29(a) and 3.29(b) duplicate Figs. 3.13(b) and 3.13(c), respectively, for the SCC4 cells in the case before Au NRI application. The complete dark image of Fig. 3.29(c) is displayed intentionally here to show the ratio mapping of the OCT signal intensity in Fig. 3.29(a) over that of the corresponding pixel in Fig. 3.29(b). It is noted that the original signal intensity in Fig. 3.13(c) or 3.29(b) has been enhanced to make the maximum ratio among pixels equal to unity. For this purpose, the signal intensity directly from the OCT scanning and processing in all the short-wavelength images based on this experiment (scanning SCC4 cells

with Au NRIs of no antibody) is enhanced by a factor of 3.15. Here, Fig. 3.29(c) is obtained by setting zero in those pixels with intensity below a threshold level in the full-spectrum image and also zero in other pixels with the aforementioned ratio smaller than or equal to unity. Based on the intensity adjustment in Fig. 3.13(c) or 3.29(b), the values in all pixels in Fig. 3.29(c) are zero and hence it shows a completely dark image. Figs.3.29(d) -3.29(f) show the OCT images, similar to Figs. 3.29(a)-3.29(c), except for the case of 24 hours after Au NRI application. Figs.3.29(d) and 3.29(f) actually duplicate Figs. 3.16(b) and 3.16(c), respectively. With Au NRIs in the cell solution, the ratio mapping in Fig. 3.29(c) is not completely dark anymore. The bright (green) spots in Fig. 3.29(c) show the distribution of Au NRI in a most conservative manner. In other words, the bright spots in Fig. 3.29(c) correspond to Au NRIs for sure. However, other Au NRIs in the cell solution may not be displayed in Fig. 3.29(c).Figs.3.29(g) -3.29(i) shows the OCT images, similar to Figs. 3.29(d) -3.29(f), except for the case after washout. In Fig. 3.29(f), one can see the settled, adsorbed (on the cell membrane), and internalized (around the cell nucleus) Au NRIs. In Fig. 3.29(i), after washout, we can more clearly see the adsorbed and internalized Au NRIs.

Figs.3.30(a)-3.30(c) show the OCT images before Au NRI application, similar to Figs. 3.29(a)-3.29(c), except for the SAS cells with antibody. Again, Fig. 3.30(c) is completely dark based on the intensity

adjustment of Fig. 3.30(b) and related Figs. by enhancing the original OCT signal intensity by 1.82. Figs.3.30(d)-3.30(f) and 3.30(g)-3.30(i) show the OCT images, similar to Figs. 3.30(a)-3.30(c), except for the cases after washout and after etching, respectively. Therefore, Fig. 3.30(f) shows the distribution of adsorbed and internalized Au NRIs and Fig. 3.30(i) shows that of only internalized Au NRIs. It is noted that in the etching processing (including another washout processing), the relative positions of cells may be moved. Hence, it is difficult to compare the cell positions in Figs. 3.30(f) and 3.30(i).

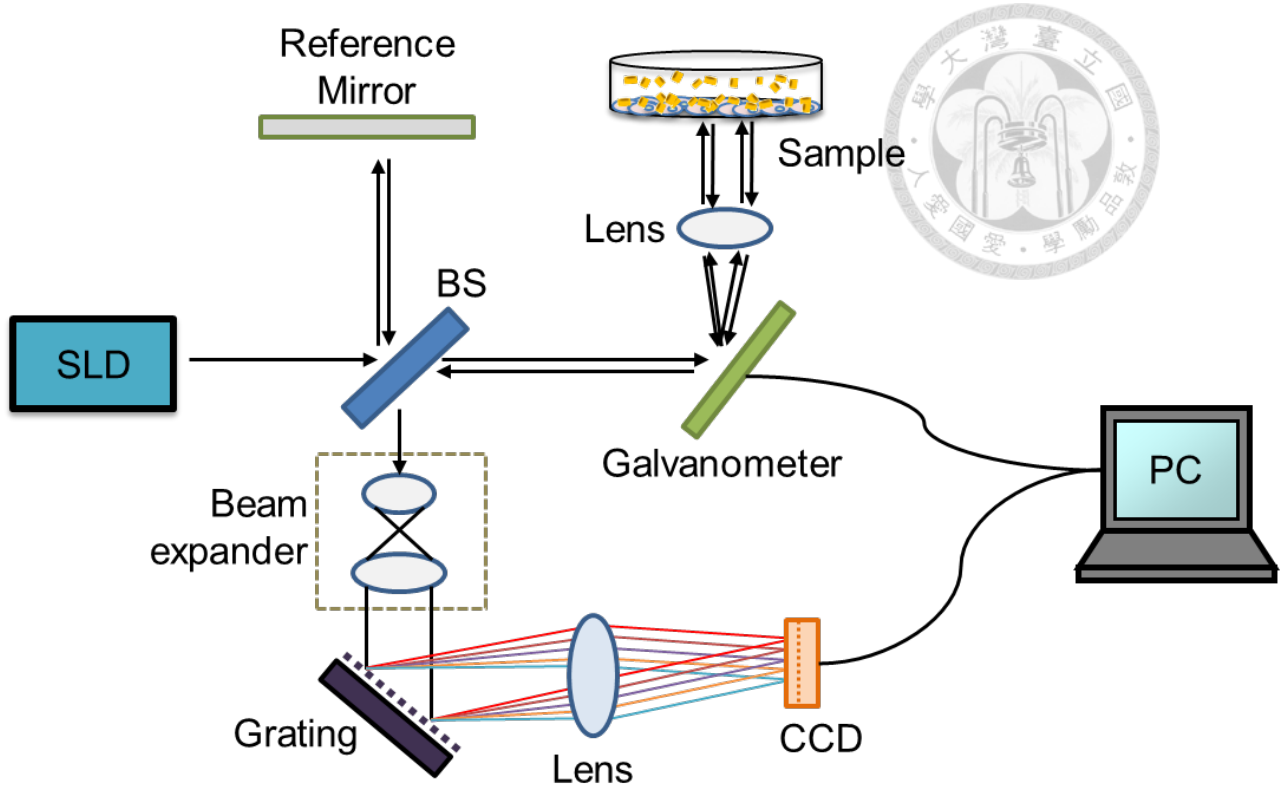

Fig. 3.1 Setup of the used OCT system.

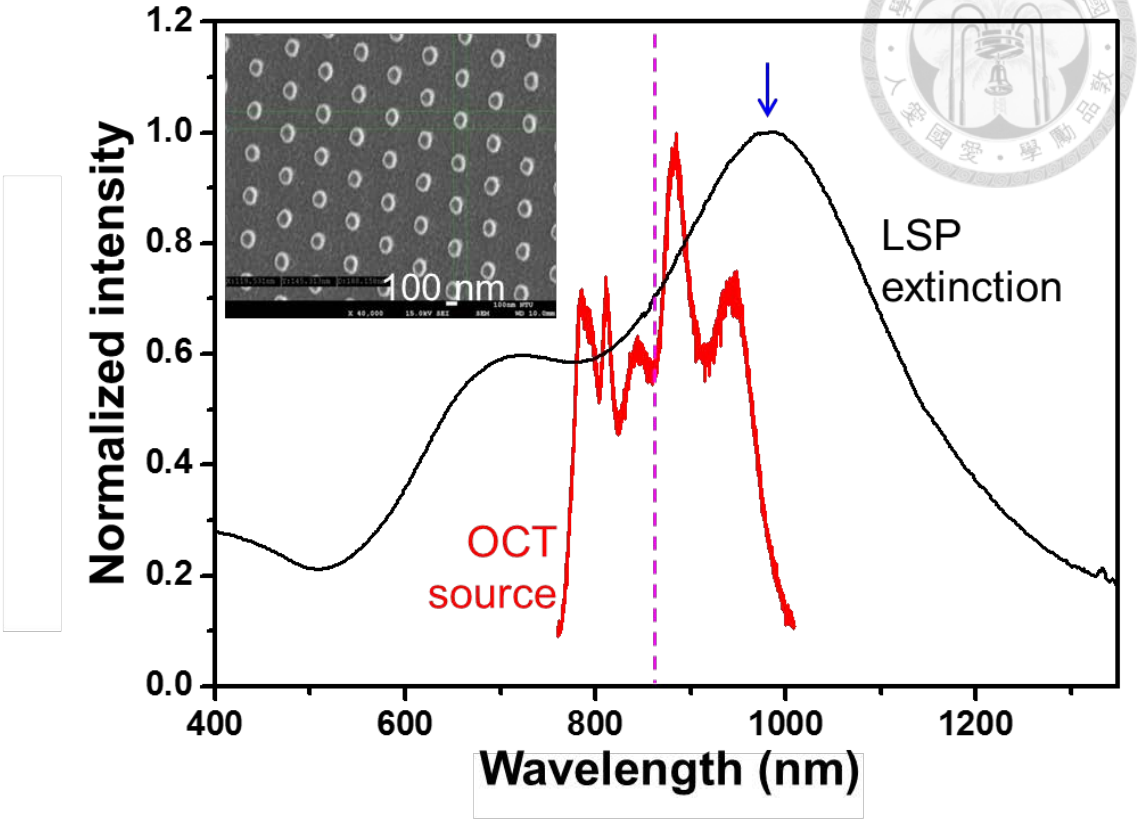

Fig. 3.2 Normalized extinction spectrum of the LSP resonance of the Au NRI solution (the black curve) and the normalized OCT light source spectrum (the red curve). The vertical dashed line at 860 nm divides the OCT source spectrum into the long- and short-wavelength halves for spectroscopic operation. The arrow indicates the LSP resonance peak of the Au NRIs in water at 980 nm. The insert shows the SEM image of the Au NRIs still on substrate.

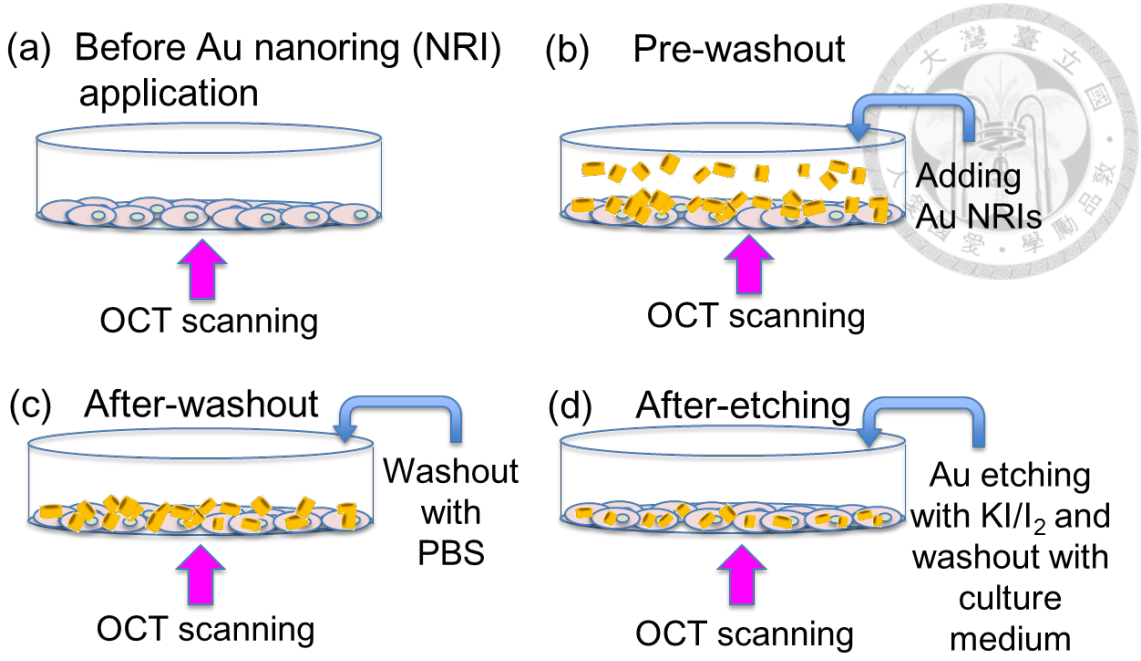

Fig. 3.3(a)-(d): Four steps of cancer cell scanning with the OCT system.

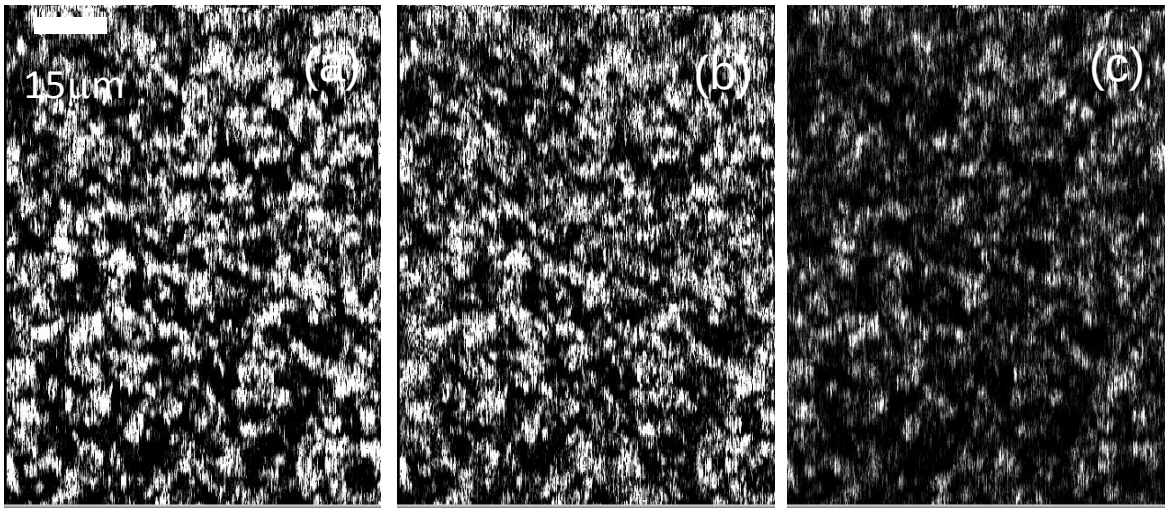

Fig. 3.4(a)-(c): OCT scanning images of Au NRI solution under the image processing conditions of full spectrum, long-wavelength portion, and short-wavelength portion, respectively.

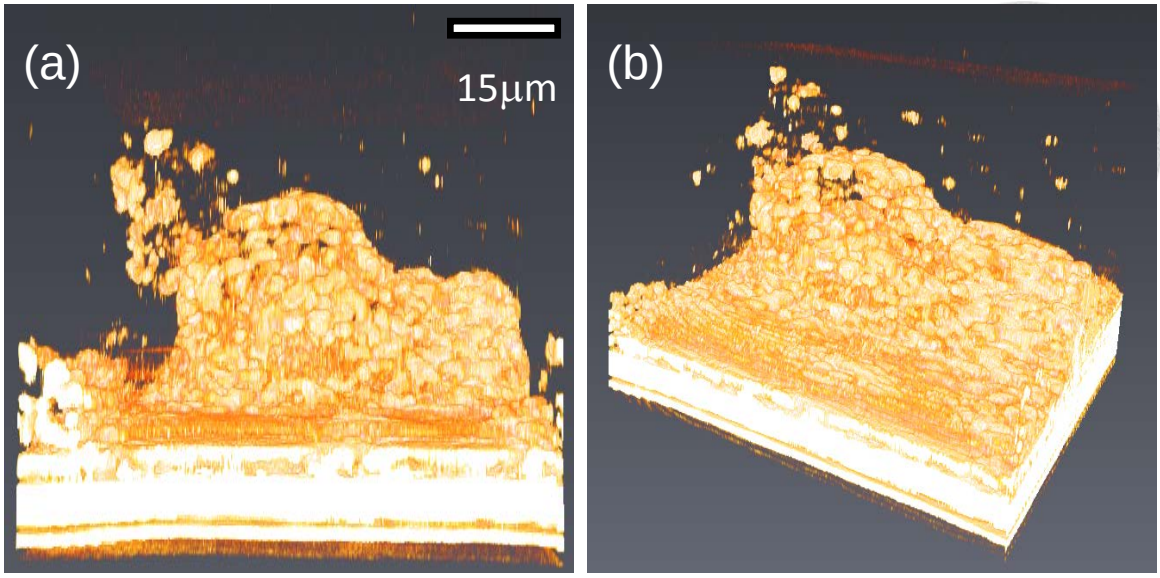

Fig. 3.5(a) and(b): 3-D OCT images of a few SCC4 cells before the application of Au NRIs.

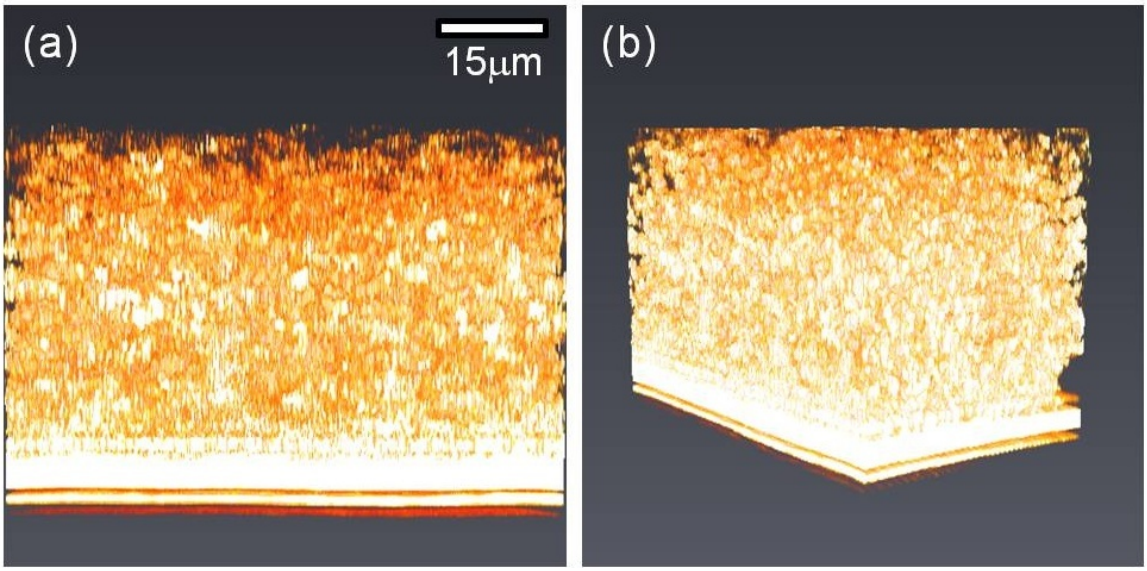

Fig. 3.6(a) and (b): 3-D OCT images of the SCC4 cells 24 hours after the application of Au NRIs.

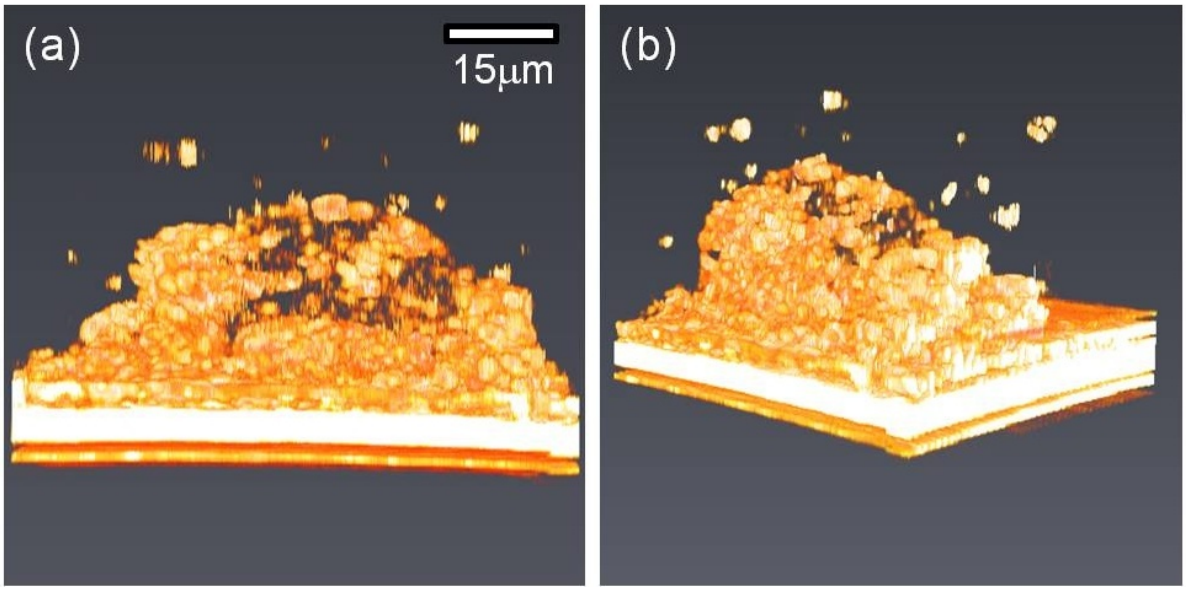

Fig. 3.7(a) and (b): 3-D OCT images of the same SCC4 cells after washout.

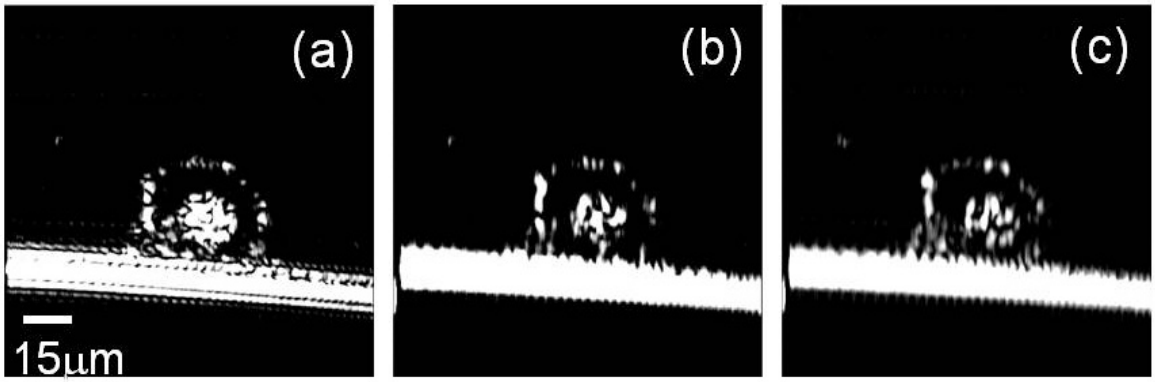

Fig. 3.8(a)-(c): B-mode OCT scanning images of an SCC4 cell under the image processing conditions of full spectrum, long-wavelength portion, and short-wavelength portion, respectively, before Au NRI application.

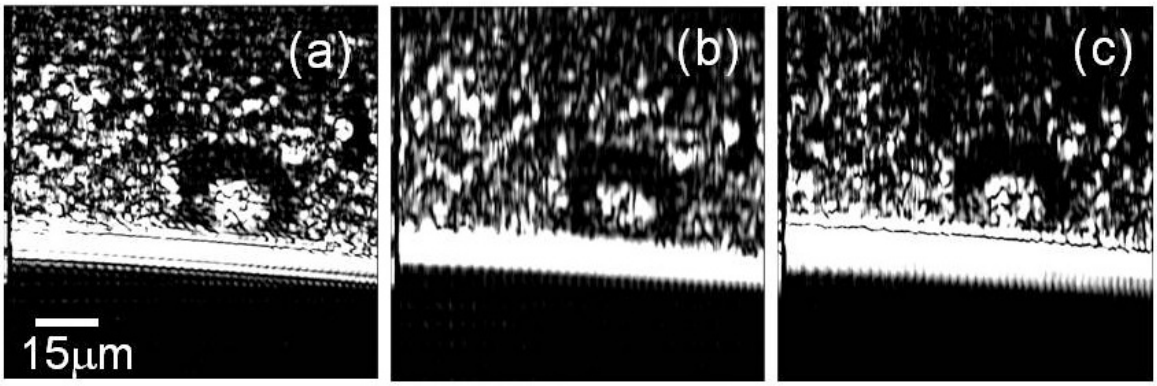

Fig. 3.9(a)-(c): B-mode OCT scanning images of the SCC4 cell, same as that in Figs. 3.8(a)-3.8(c), under the image processing conditions of full spectrum, long-wavelength portion, and short-wavelength portion, respectively, 6 hours after the Au NRIs are added to the cell solution.

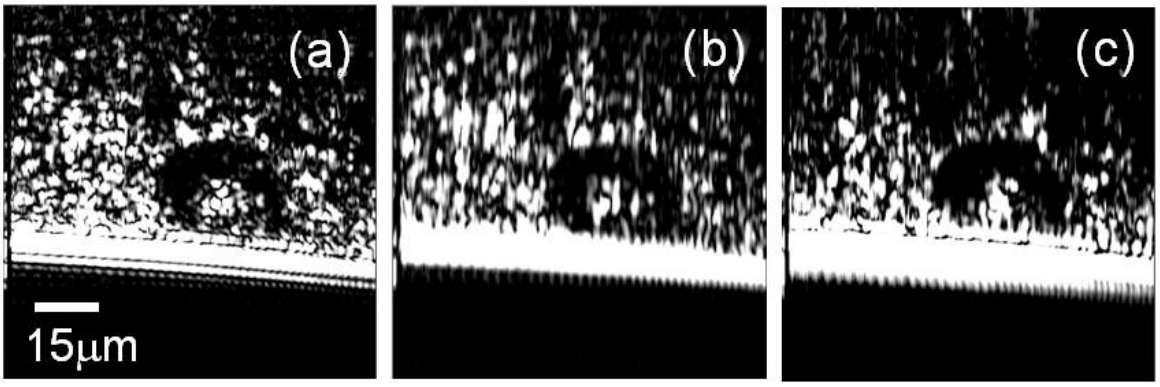

Fig. 3.10(a)-(c): B-mode OCT scanning images of the SCC4 cell under the image processing conditions of full spectrum, long-wavelength portion, and short-wavelength portion, respectively, 12 hours after the Au NRIs (without antibody) are added to the cell solution.

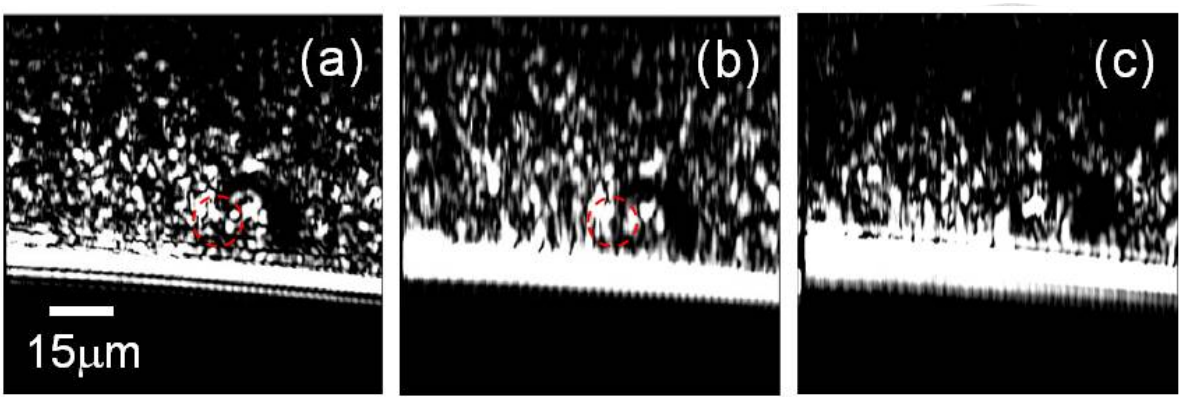

Fig. 3.11(a)-(c): B-mode OCT scanning images of the SCC4 cell under the image processing conditions of full spectrum, long-wavelength portion, and short-wavelength portion, respectively, 24 hours after the Au NRIs are added to the cell solution.

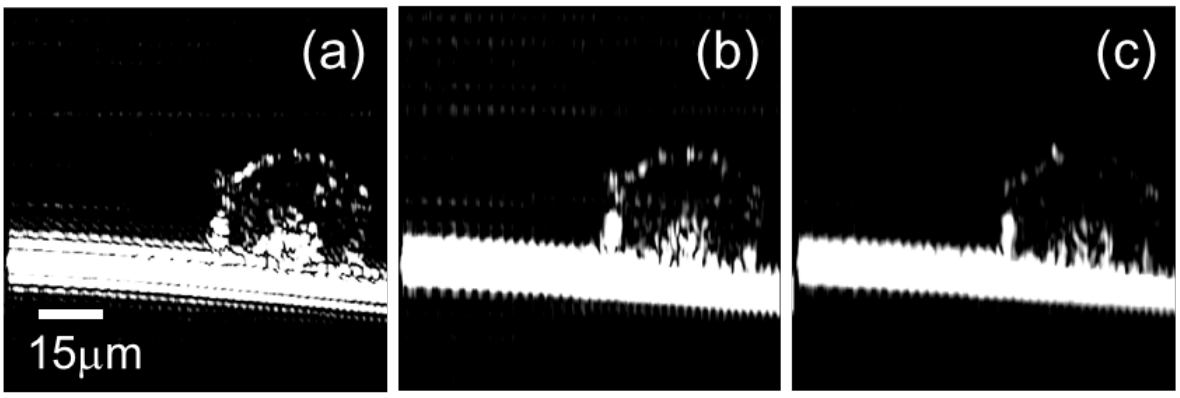

Fig. 3.12(a)-(c): B-mode OCT scanning images of the SCC4 cell under the image processing conditions of full spectrum, long-wavelength portion, and short-wavelength portion, respectively, after the washout of Au NRIs.

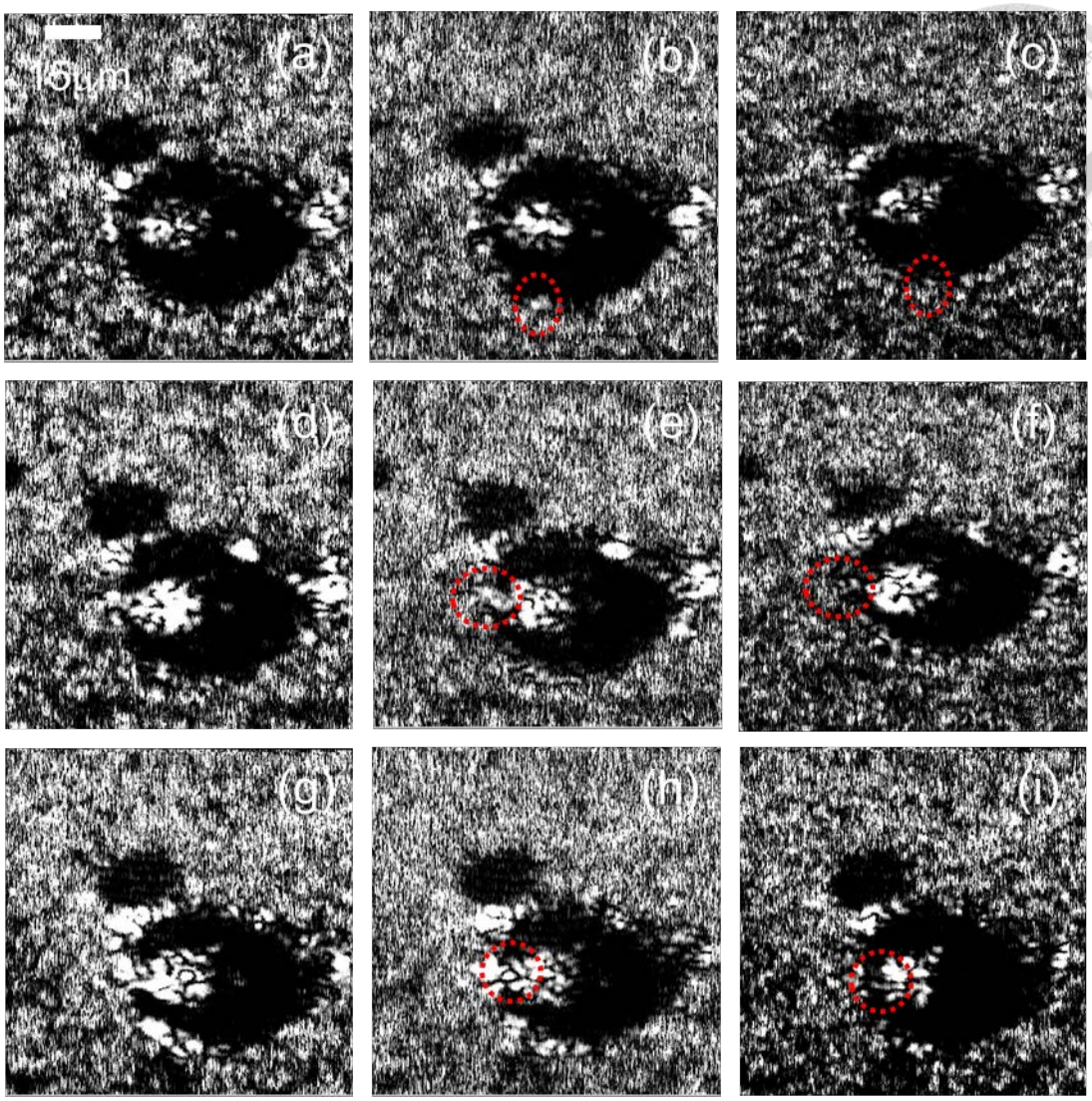

Fig. 3.13(a)-(c) ((d)-(f) and (g)-(i)): En-face OCT scanning images of a SCC4 cell under the image processing conditions of full spectrum, long-wavelength portion, and short-wavelength portion, respectively, before Au NRI application (2 and 10 hours, respectively, after Au NRI application).

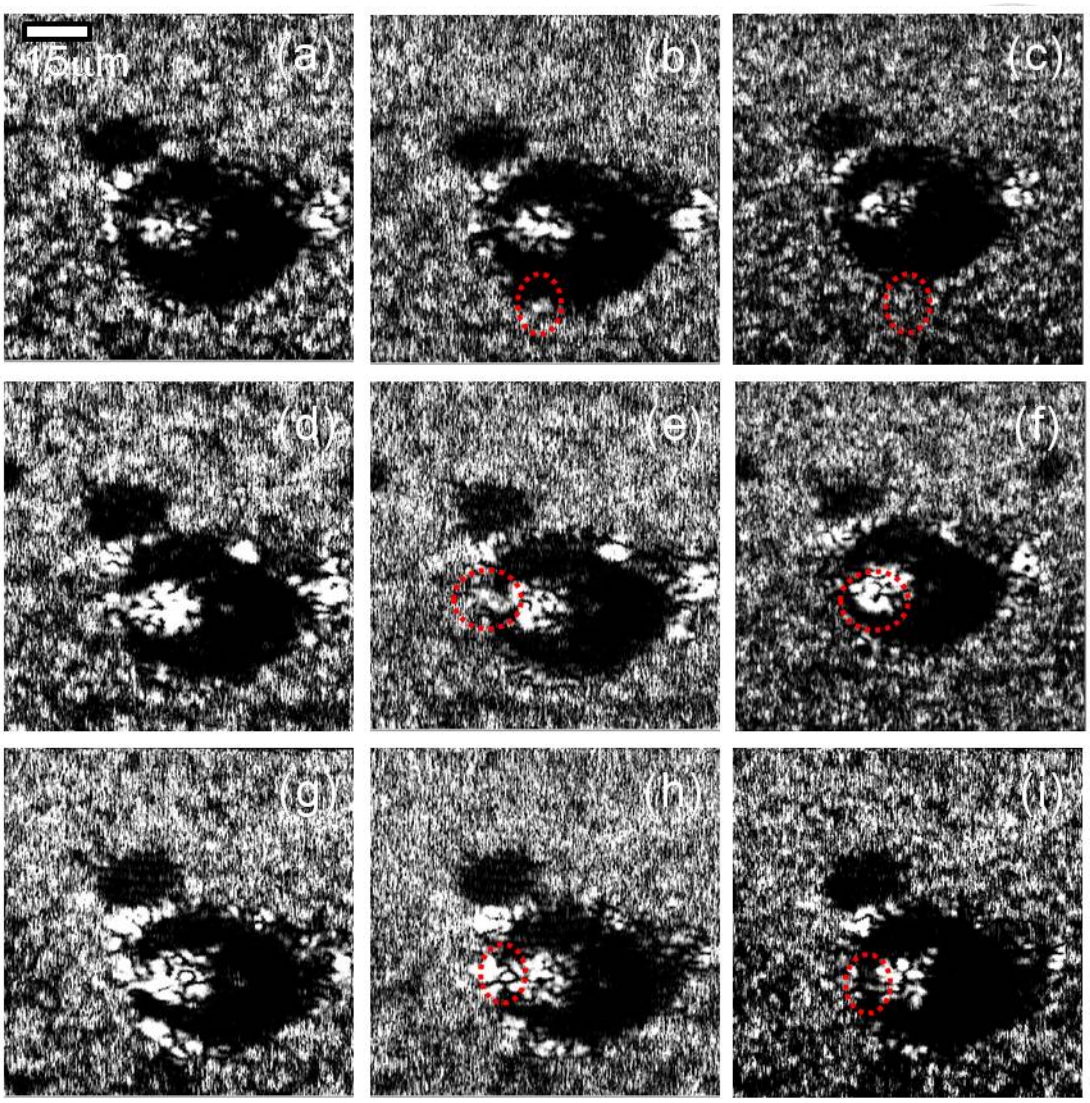

Fig. 3.14 (a)-(c) ((d)-(f) and (g)-(i)) : En-face OCT images, similar to those in Figs. 3.13(g) -3.13(i), respectively, 11 (12 and 13, respectively) hours after Au NRI application.

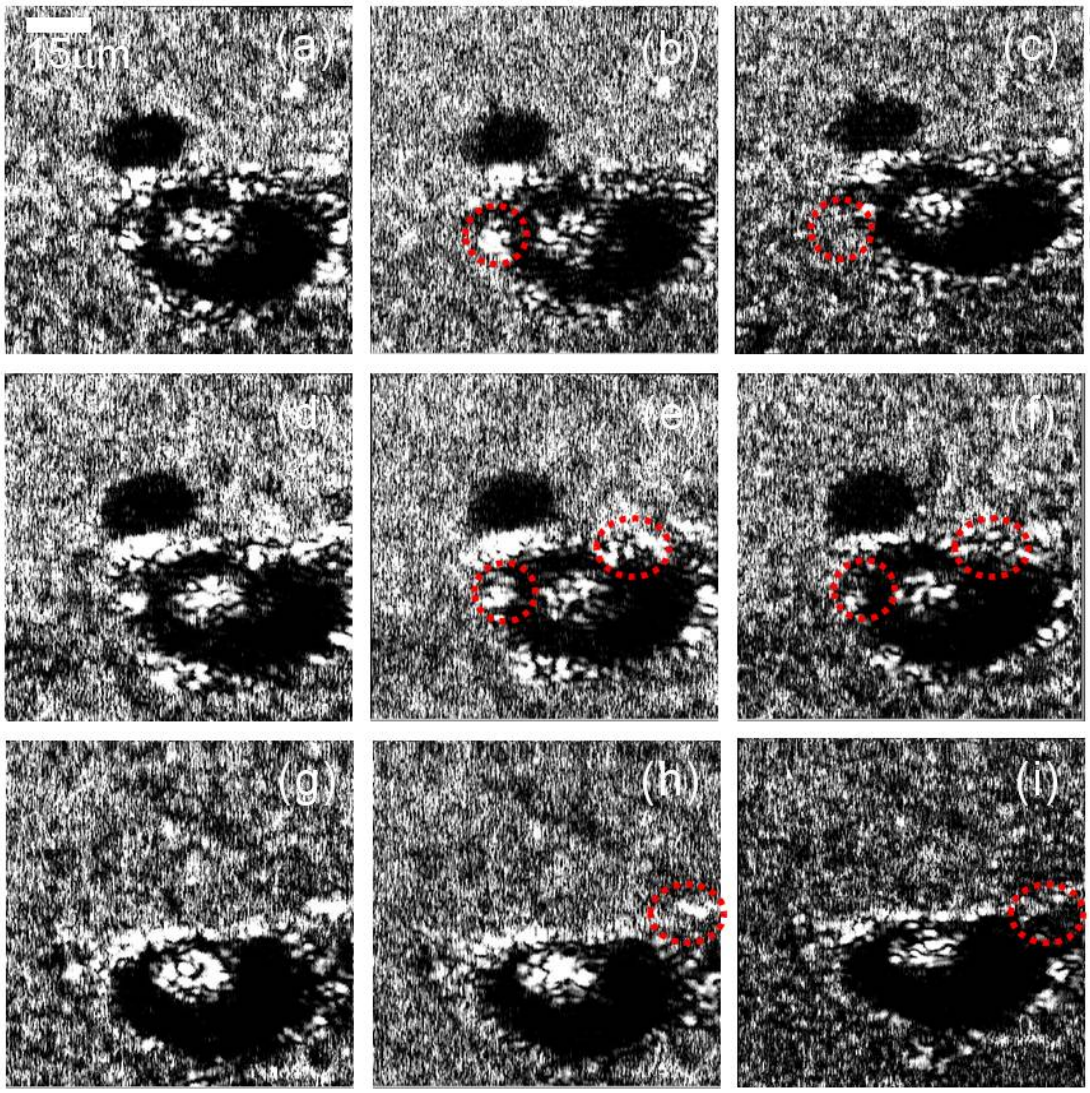

Fig. 3.15 (a)-(c) ((d)-(f) and (g)-(i)) : En-face OCT images, similar to those in Figs. 3.14(g)-3.14(i), respectively, 16 (17 and 23, respectively) hours after Au NRI application.

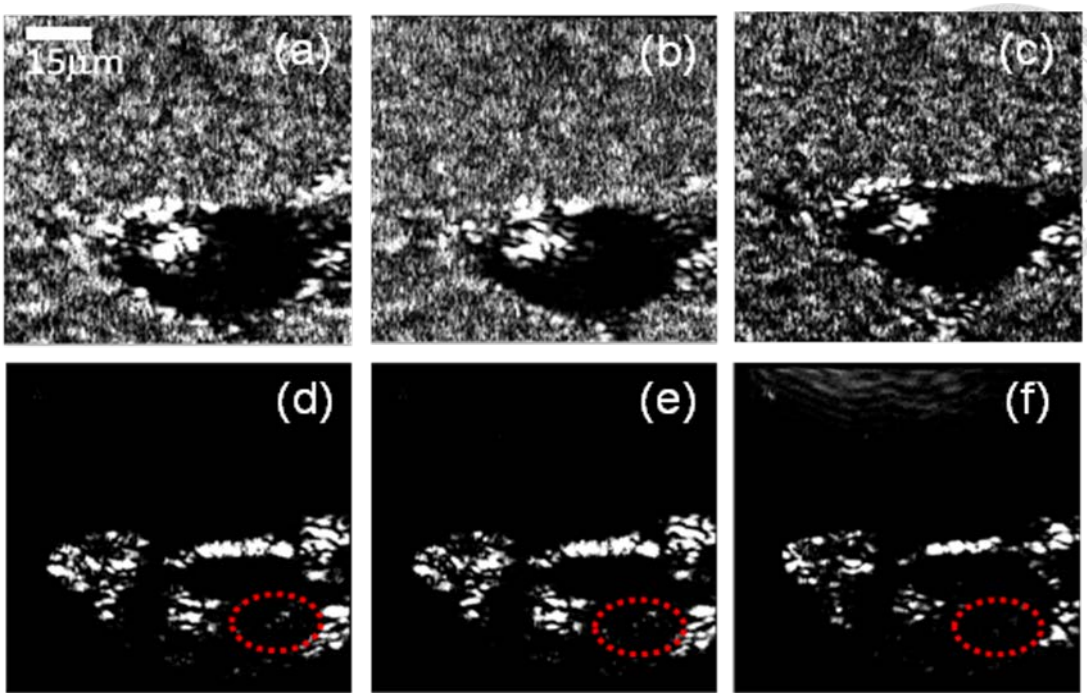

Fig. 3.16 (a)-(c) ((d)-(f)): En-face OCT images, similar to those in Figs. 3.15(g) -3.15(i), respectively, 24 hours after Au NRI application (after washout).

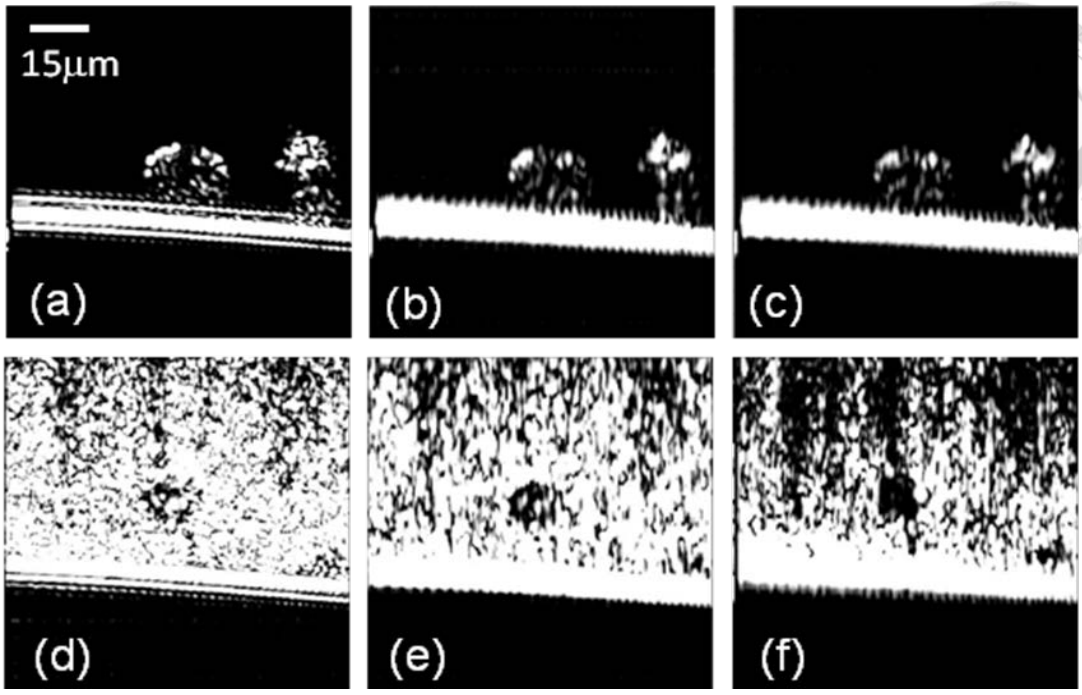

Fig. 3.17(a)-(c) ((d)-(f)): B-mode OCT scanning images of two or more SCC4 cells under the image process conditions of full spectrum, long-wavelength portion, and short-wavelength portion, respectively, before Au NRI (with antibody) application (24 hours after Au NRI application).

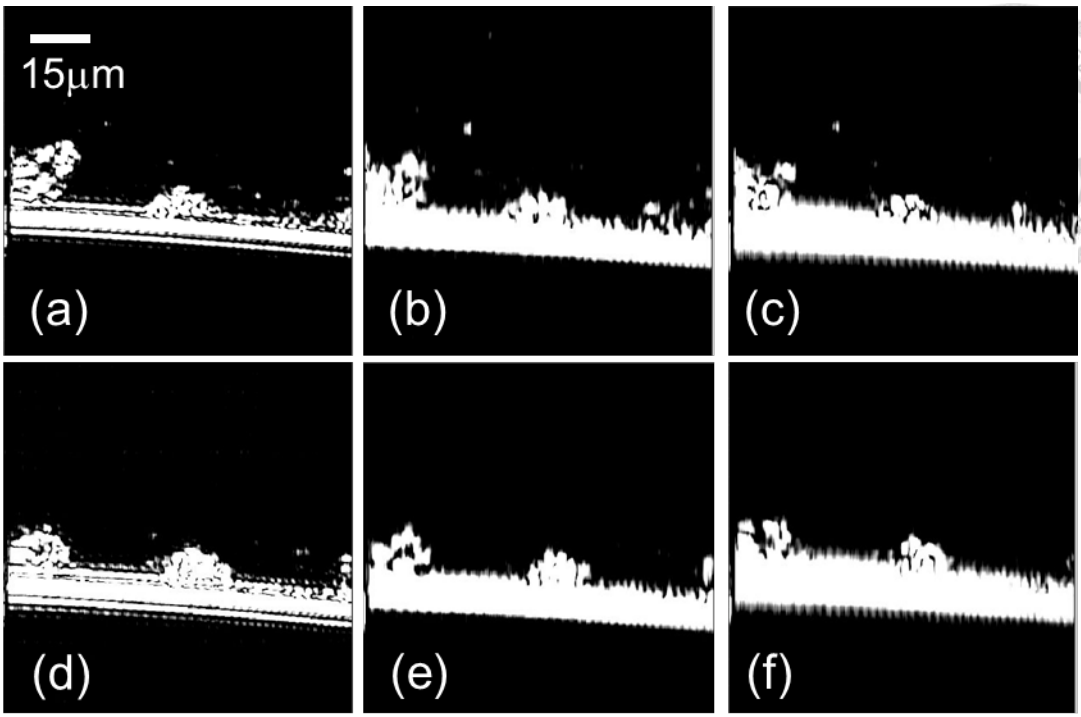

Fig. 3.18(a)-(c) ((d) -(f)) : B-mode OCT images, similar to those in Figs. 3.17(a) -3.17(c), respectively, after washout (after etching).

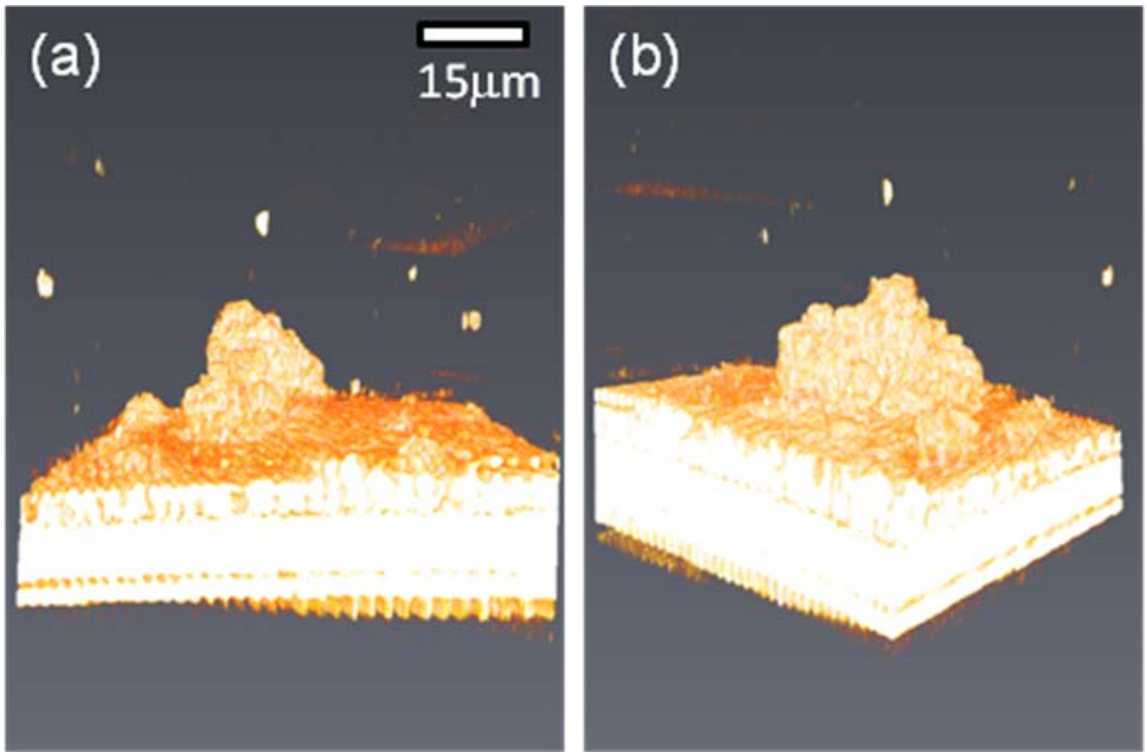

Fig. 3.19(a) and (b): 3-D OCT images of one or two SAS cells before the application of Au NRIs (with antibody linkage).

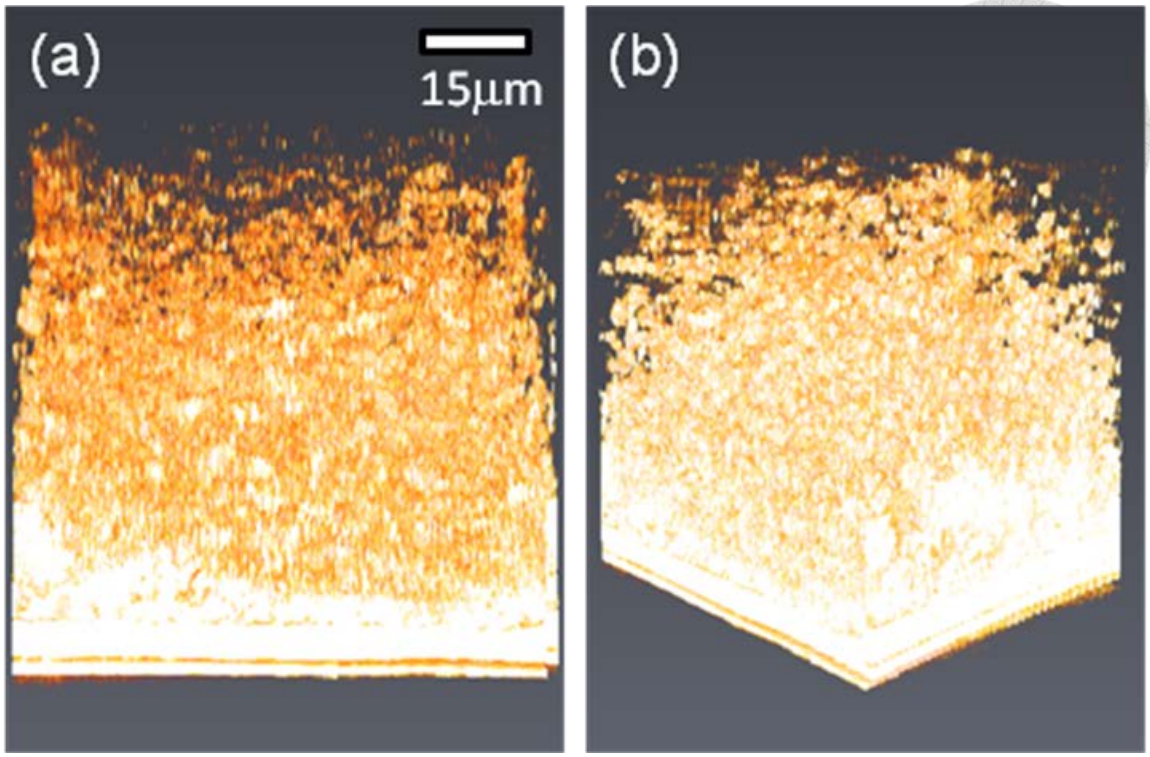

Fig. 3.20(a)and (b): 3-D OCT images of the same SAS cells 24 hours after the application of Au NRIs.

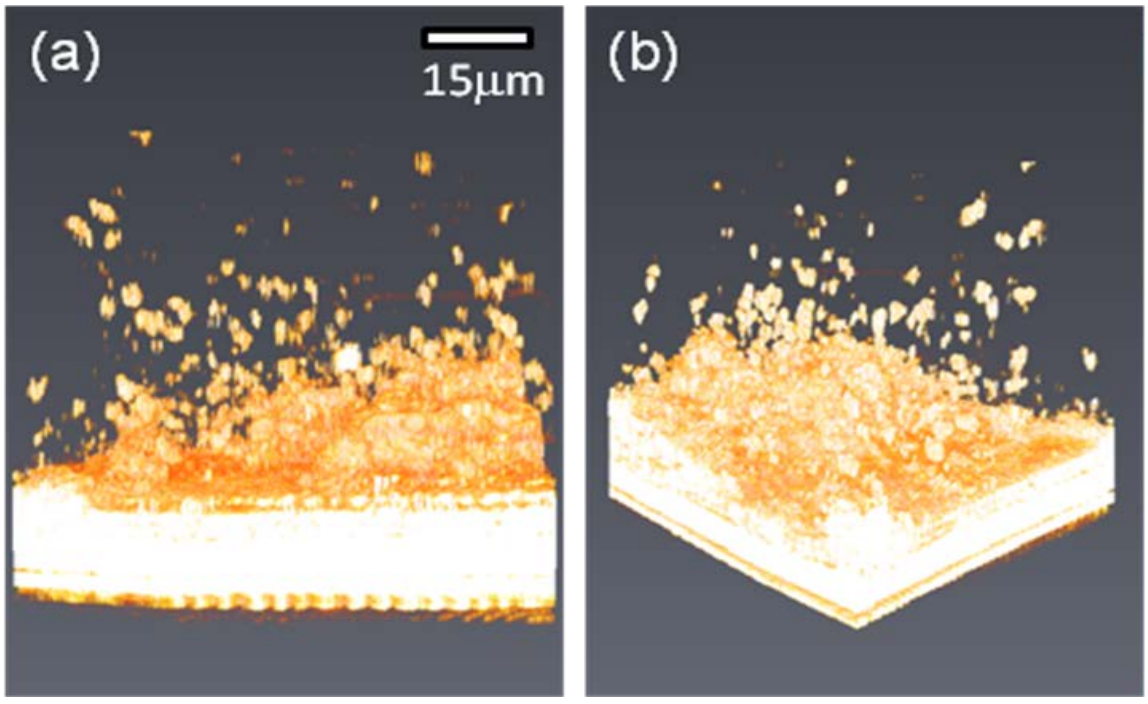

Fig. 3.21(a) and (b): 3-D OCT images of the same SAS cells after washout.

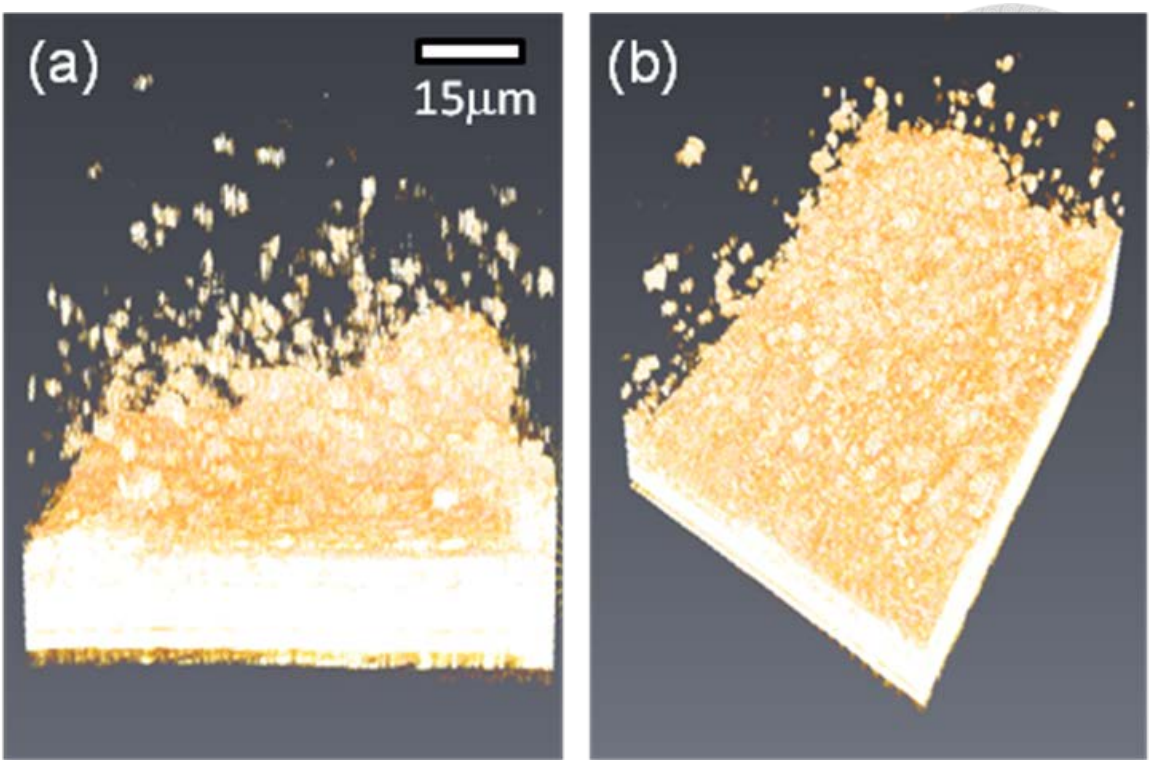

Fig. 3.22(a) and (b): 3-D OCT images of the same SAS cells after etching.

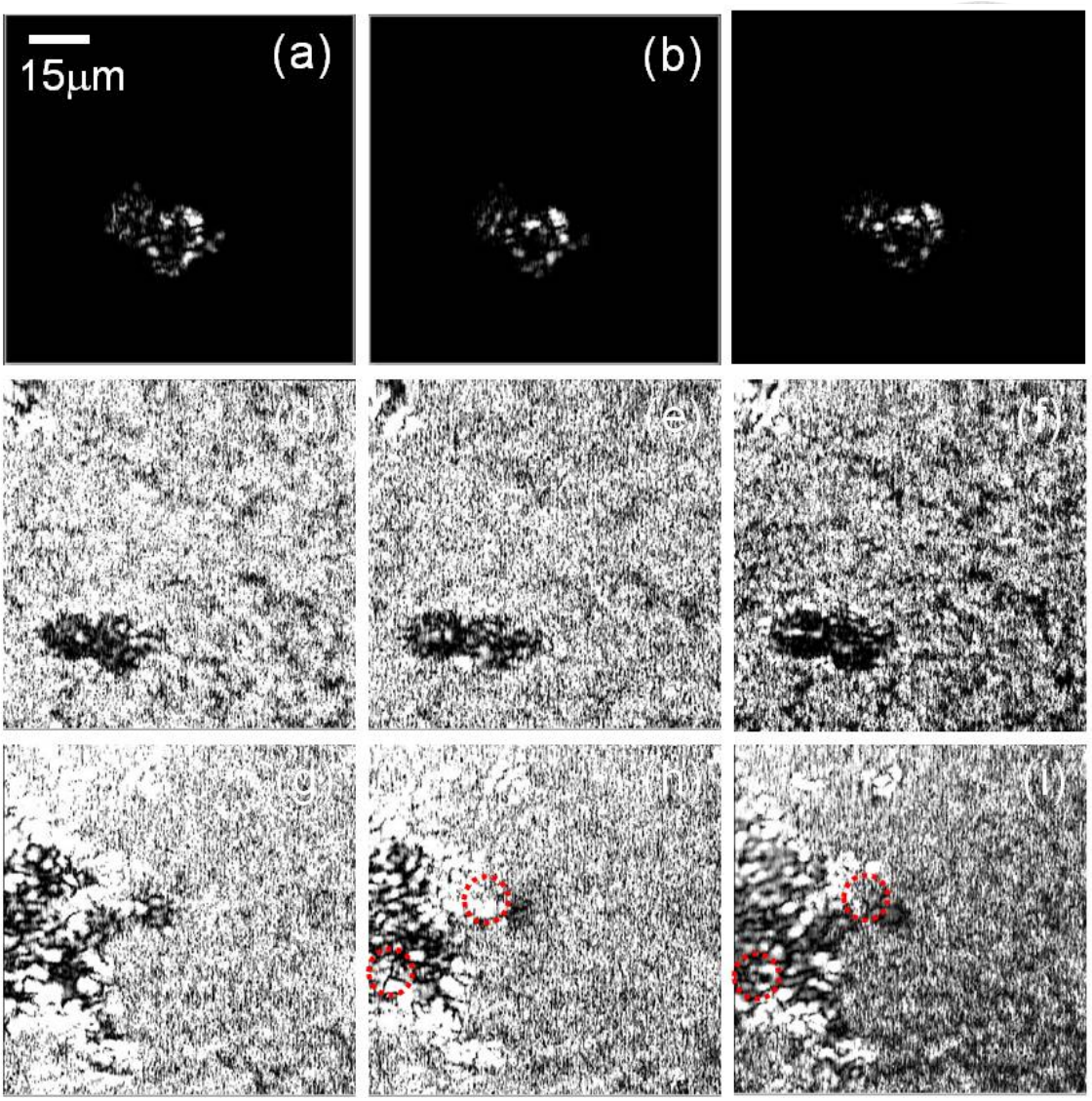

Fig. 3.23(a)-(c) ((d)-(f) and (g)-(i)) : En-face OCT scanning images of two attached SAS cells under the image processing conditions of full spectrum, long-wavelength portion, and short-wavelength portion, respectively, before Au NRI application (3 and 15 hours, respectively, after Au NRI application).

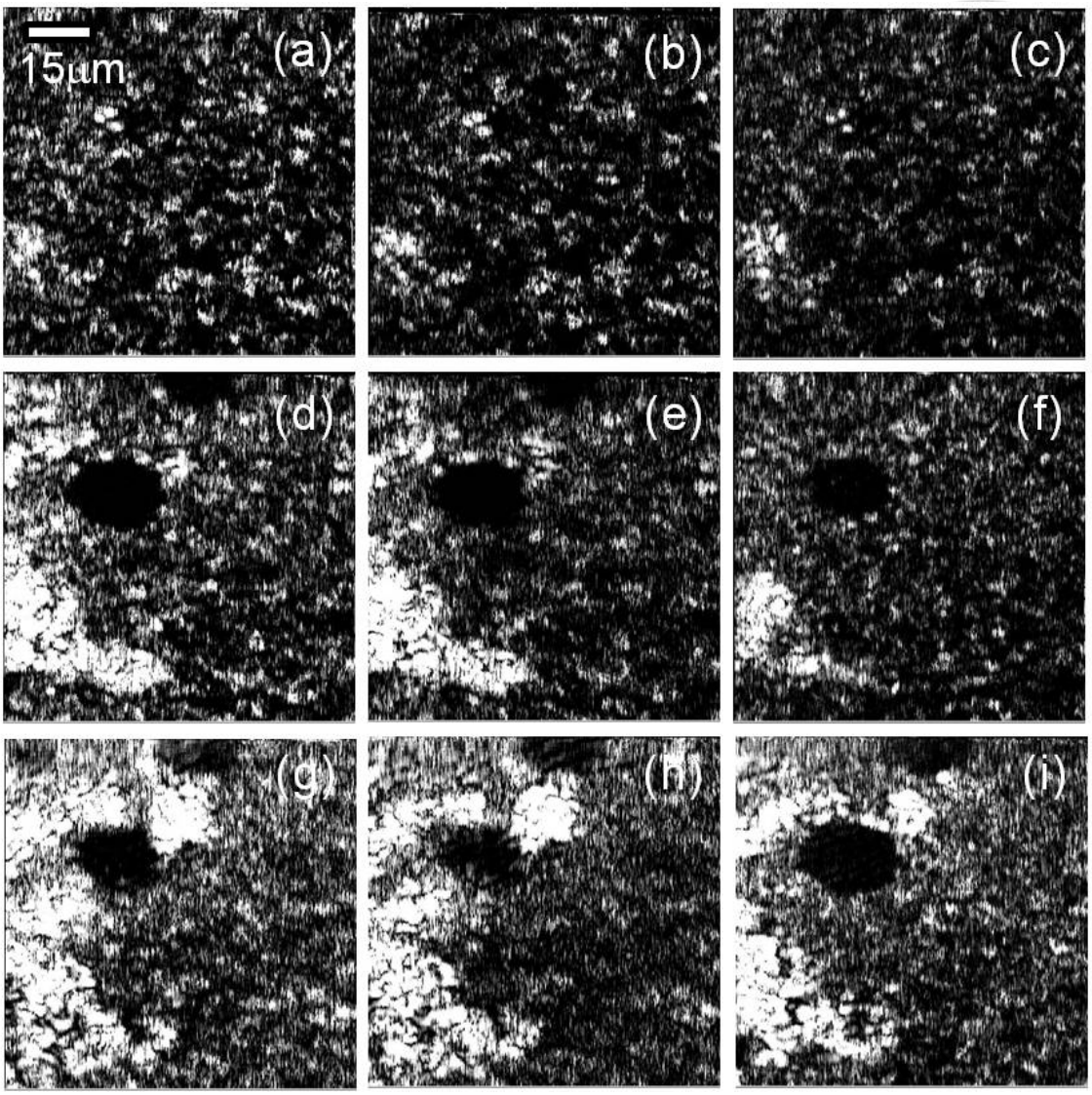

Fig. 3.24(a)-(c), (d)-(f), and (g)-(i): En-face OCT images of the same lateral region as that in Fig. 3.23 at different depths under the image processing conditions of full spectrum, long-wavelength portion, and short-wavelength portion, respectively, 24 hours after Au NRI application. The images in the second (third) row correspond to the depth 7 microns deeper than those in the first (second) row.

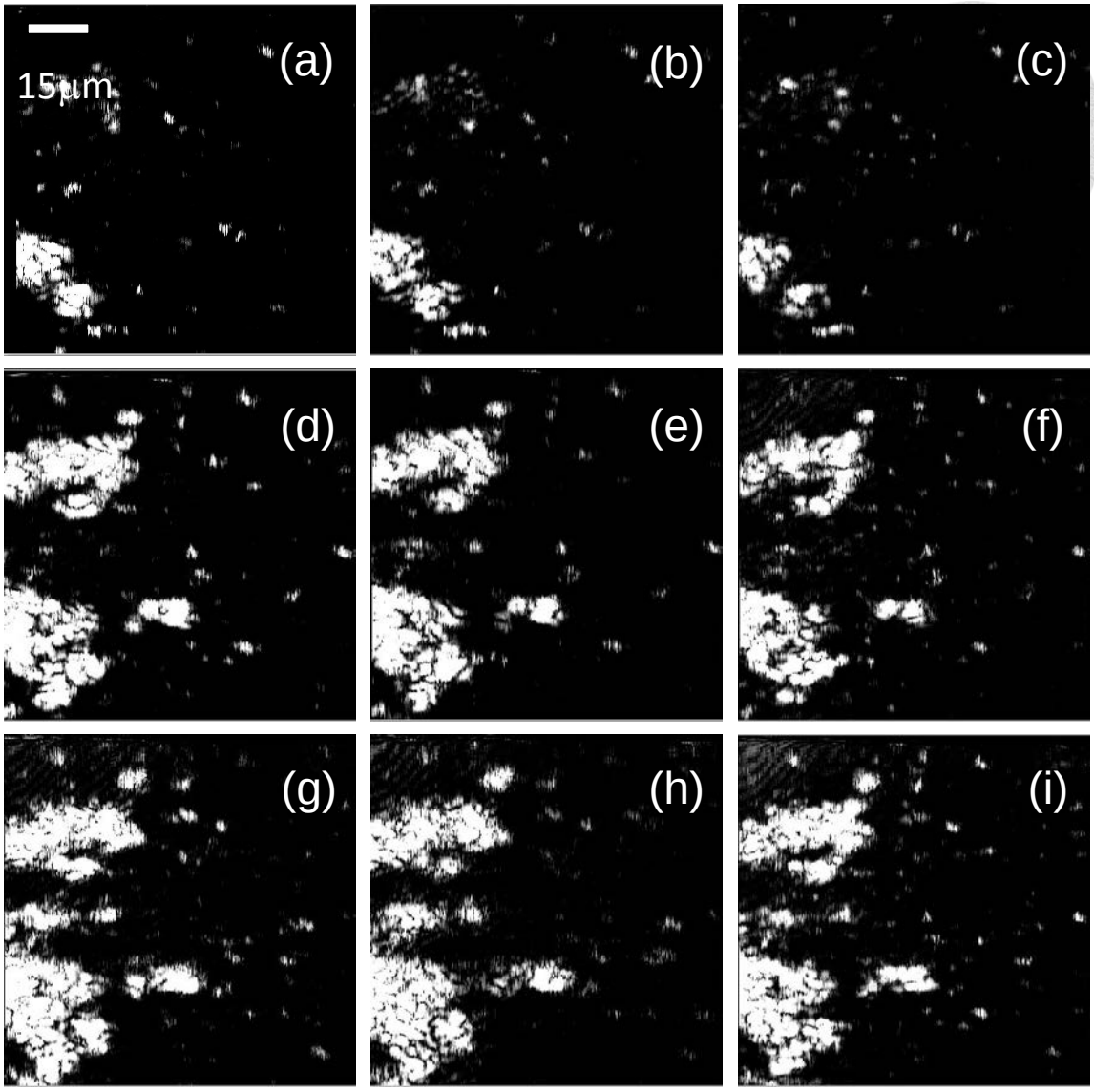

Fig. 3.25(a)-(i): En-face OCT images corresponding to those in Figs. 3.24(a)-3.24(i), respectively, after washout.

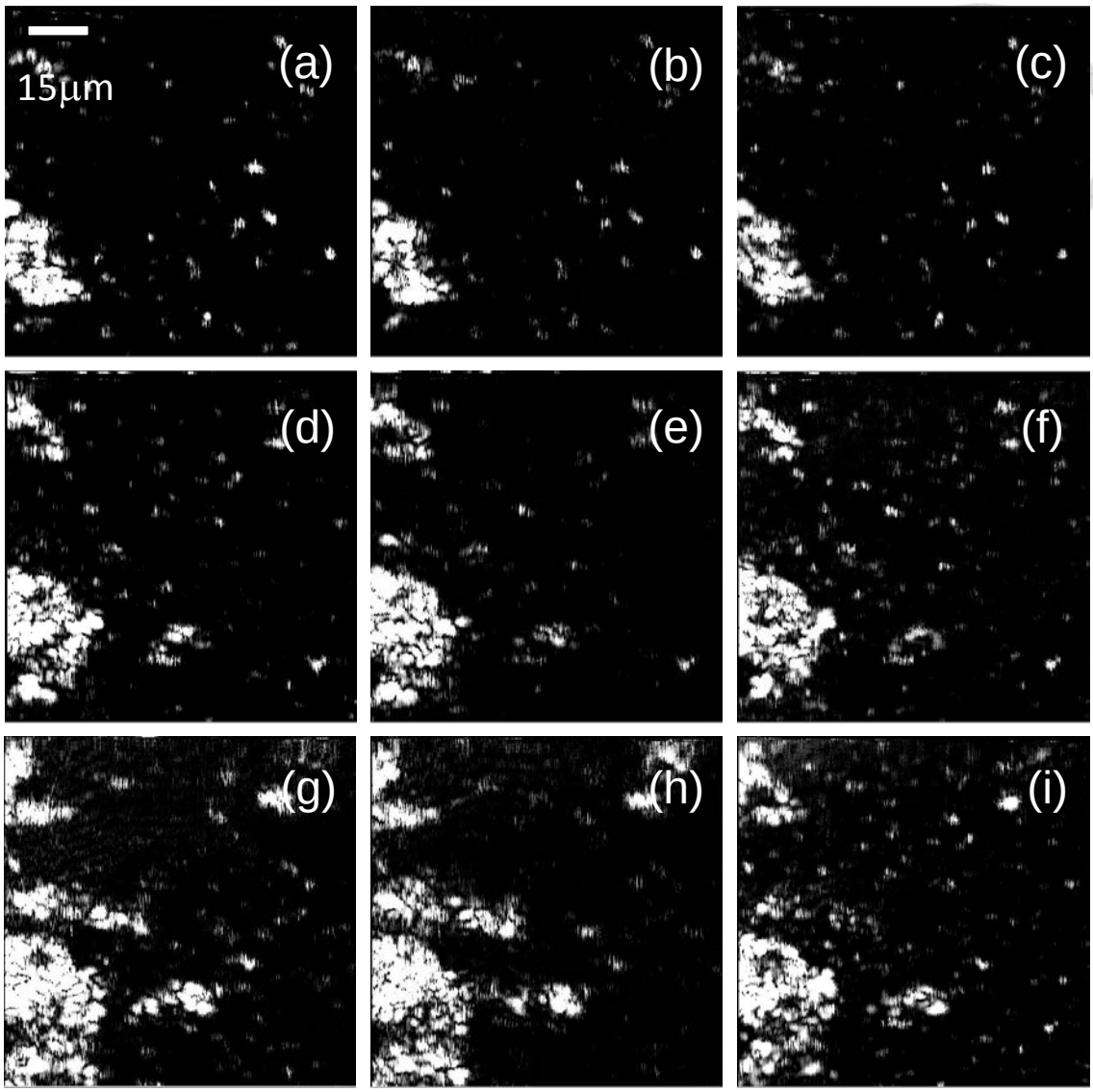

Fig. 3.26 (a)-(i): En-face OCT images corresponding to those in Figs. 3.25(a)-3.25(i), respectively, after etching.

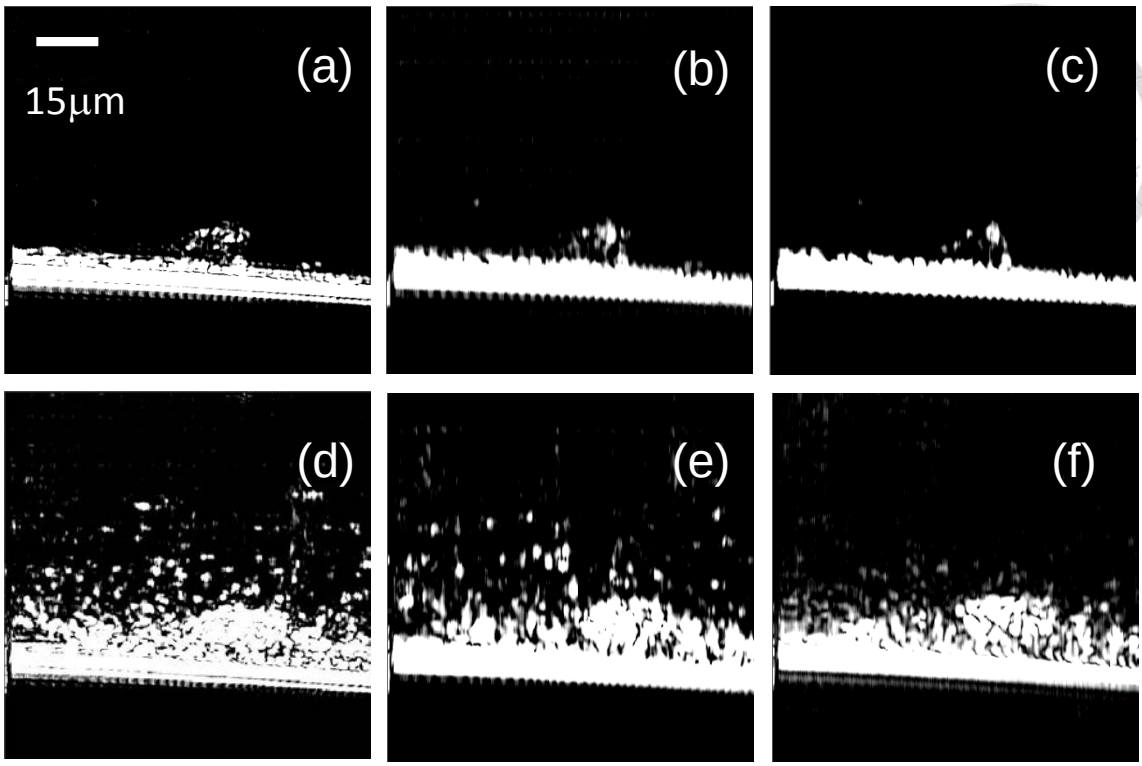

Fig. 3.27 (a)-(c) and (d)-(f): B-mode OCT scanning images of one or more SAS cells under the image processing conditions of full spectrum, long-wavelength portion, and short-wavelength portion, respectively, before Au NRI application and 24 hours after Au NRI application, respectively.

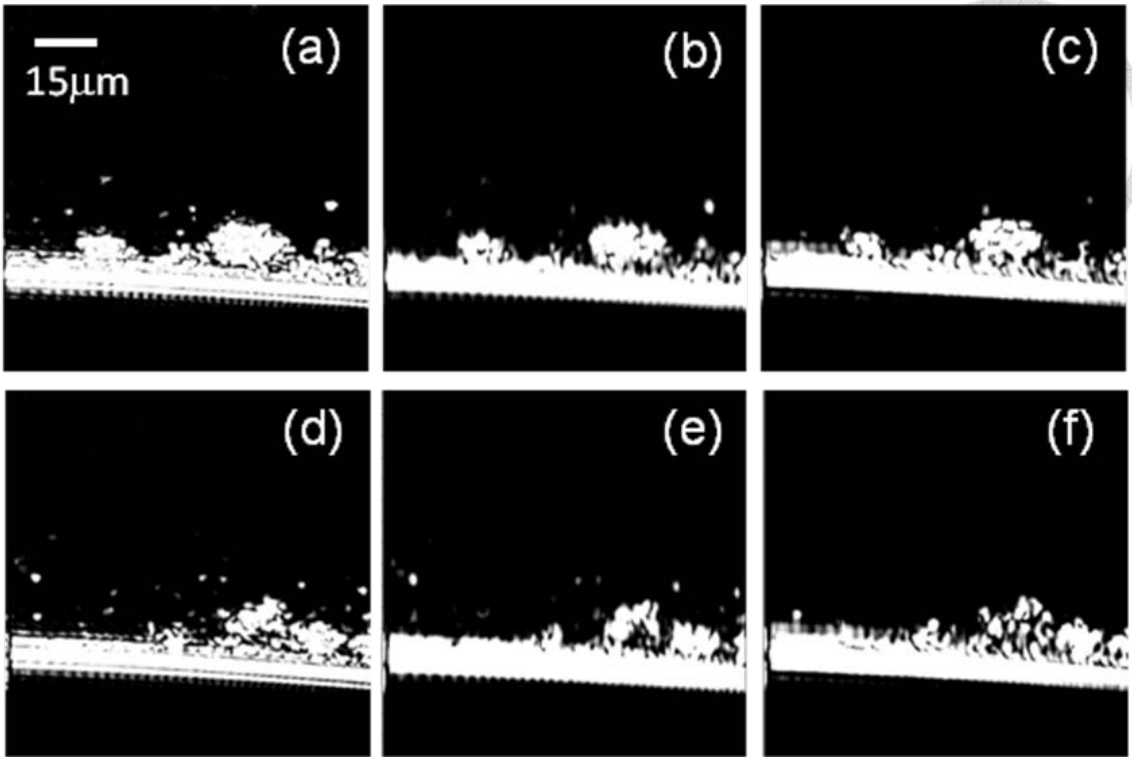

Fig. 3.28 (a)-(c) and (d)-(f) : B-mode OCT scanning images of one or more SAS cells under the image processing conditions of full spectrum, long-wavelength portion, and short-wavelength portion, respectively, after washout and after etching, respectively.

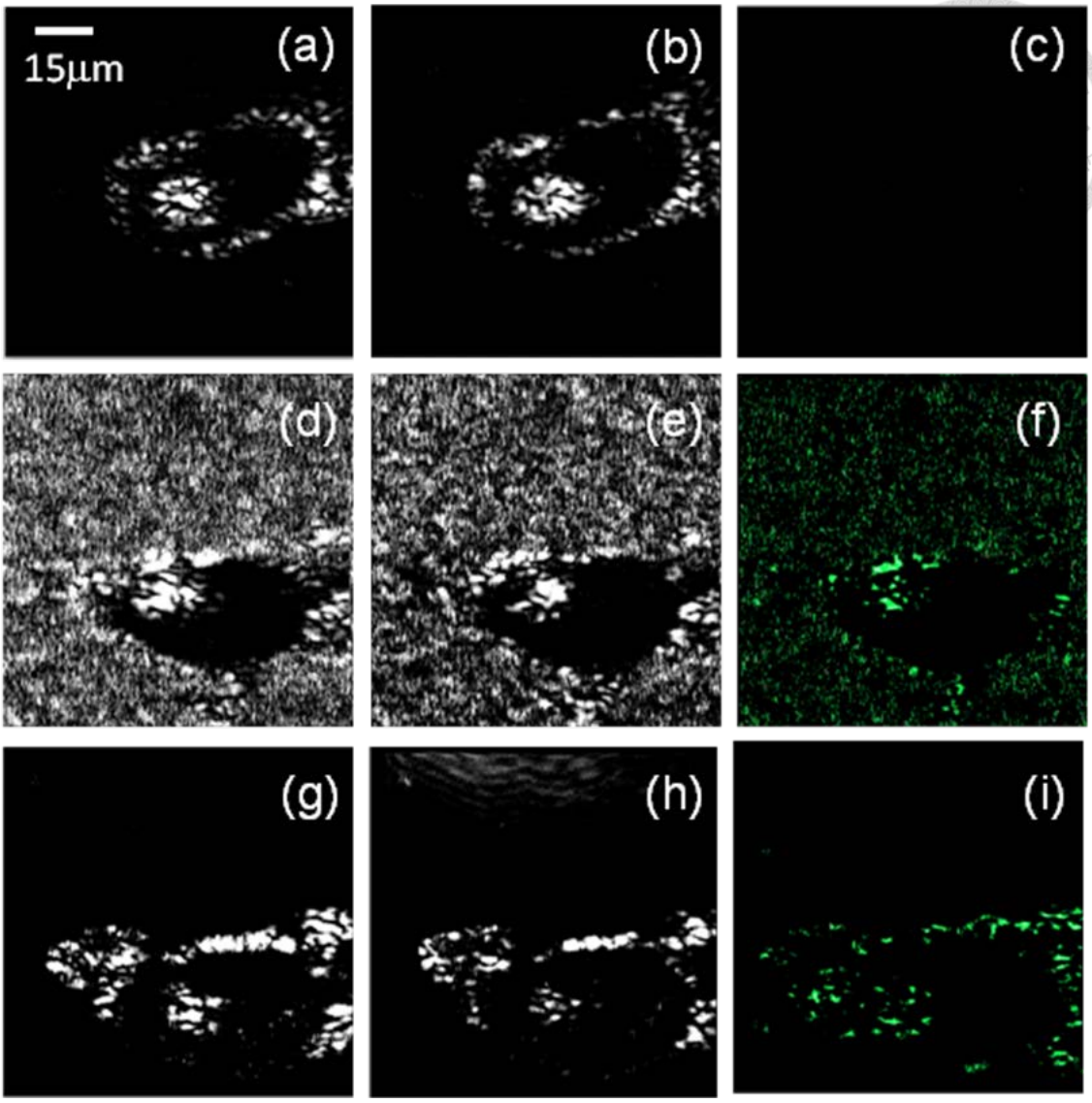

Fig. 3.29 (a) and (b): Long- and short-wavelength images of the SCC4 cells before Au NRI (without antibody) application. (c): Ratio mapping of part (a) over part (b). (d)-(f): OCT images, similar to parts (a) - (c), except for the case of 24 hours after Au NRI application. (g)-(i): OCT images, similar to parts (d)-(f), except for the case after washout.

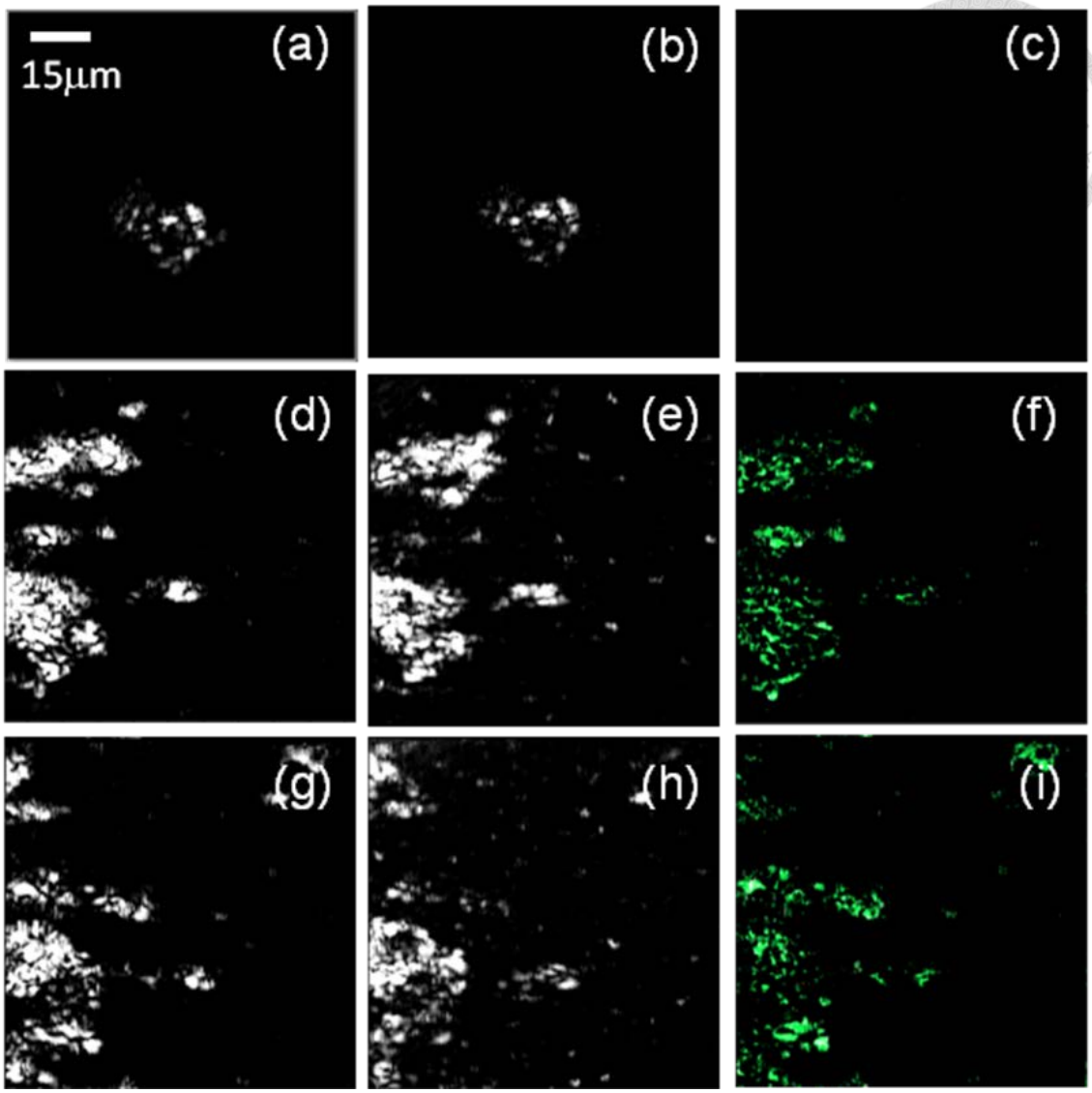

Fig. 3.30 (a) and (b): Long- and short-wavelength images of the SAS cells before Au NRI (with antibody) application. (c): Ratio mapping of part (a) over part (b). (d)-(f): OCT images, similar to parts (a)-(c), except for the case after washout. (g)-(i): OCT images, similar to parts (d)-(f), except for the case after etching.

Chapter 4

Conclusions

In summary, we have built a spectral-domain OCT system with a light source of ~200 nm in spectral width to achieve the depth and lateral resolutions of ~2 and <4 microns, respectively. This OCT system was used for scanning two kinds of human oral cancer cells (SCC4 and SAS) with applied Au NRIs. The LSP resonance behavior of the Au NRIs, which resulted in strong scattering of the Au NRIs for OCT imaging, was well controlled such that the long- and short-wavelength halves of the OCT source spectrum had different LSP resonance strengths. Based on this spectral distribution, the spectroscopic operation of the OCT system could lead to the different imaging intensities of the Au NRI distribution in the cell solution between the long- and short-wavelength images. OCT scans were performed at four stages of cell solution, including those before the application of Au NRIs, after the application of Au NRIs, after the washout of the Au NRIs not adsorbed or internalized by the cells, and after the etching of the Au NRIs not internalized by the cells. From the OCT images, particularly the differences between the long- and short-wavelength images in the spectroscopic operation, one could identify the adsorbed and internalized Au NRIs by the cells. It was found

that with antibody linkage to the Au NRIs, the Au NRI adsorption and internalization efficiencies became higher.

References

[1] D. Huang, E. A. Swanson, C. P. Lin, J. S. Schuman, W. G. Stinson, W. Chang, M. R. Hee, T. Flotte, K. Gregory, C. A. Puliafito, and J. G. Fujimoto, Science**254**, 1178 (1991).

[2] D.C. Adler, Y. Chen, R. Huber, J. Schmitt, J. Connolly, and J. C. Fujimoto, Nature Photonics**1**, 709 (2007).

[3] S. H. Yun, G. J. Tearney, J. F. de Boer, N. Iftimia, and B. E. Bouma, Opt. Express**11**, 2953 (2003).

[4] B. Cense, N. Nassif, T. Chen, M. Pierce, S. H. Yun, B. Park, B. Bouma, G. Tearney, and J. de Boer, Opt. Express **12**, 2435 (2004).

[5] R. Huber, M. Wojtkowski, and J. G. Fujimoto, Opt. Express **14**,225 (2006).

[6] R. Huber, D. C. Adler, and J. G. Fujimoto, Opt. Lett. **31**, 2975 (2006).

[7] M. R.Hee, J. A. Izatt, E. A. Swanson, D. Huang, J. S. Schuman, C. P. Lin, C. A. Puliafito, and J. G. Fujimoto, Arch. Ophthalmology**113**, 326 (1995).

[8] J. S. Schuman, P. K. Tamar, E.Hertzmark, M. R. Hee, J. R. Wilkins, J.G. Coker, C. A. Puliafito, J. G. Fujimoto, and E. A. Swanson, Ophthalmology**103**, 1889 (1996).

[9] M. R. Hee, C. A. Puliafito, J.S. Duker, E. Reichel, J. G. Coker, J. R. Wilkins, J.S. Schuman, E. A. Swanson, and J. G. Fujimoto, Ophthalmology**105**, 360 (1998).

[10] W. Drexler, U.Morgner, R. K. Ghanta, F. X. Kärtner, J. S. Schuman, and J. G. Fujimoto, Nature Medicine**7**, 501 (2001).

[11] J.S. Schuman, C.A. Puliafito, and J.G. Fujimoto, Optical coherence tomography of ocular diseases, 2nd edition. Thorofare, NJ: Slack Inc.; 2004.

[12] B.H. Park, C. Saxer, S.M. Srinivas, J.S. Nelson, and J.F. de Boer, J. Biomed. Opt. **6**, 474 (2001).

[13] S. Jiao, W. Yu, G. Stoica, and L.V. Wang, Appl. Opt. **42**, 5191(2003).

[14] S. M. Srinivas, J. F. D. Boer, and H. Park, J. Biomed. Opt. **9**, 207(2004).

[15] G.J. Tearney, M.E. Brezinski, J.F. Southern, B.E. Bouma, S.A. Boppart, and J.G. Fujimoto, Am J Gastroenterol. **92**, 1800 (1997).

[16] M.V. Sivak, K. Kobayashi,J.A. Izatt, et al., GastrointestEndosc. **51,**474(2000).

[17] A.R. Tumlinson, B. Povazay, L.P. Hariri, et al., J. Biomed. Opt. **11**, 064003 (2006).

[18] Y. Yang, S. Whiteman, D. G. Pittius, Y. He, R.K. Wang, and M.A. Spiteri,Phys. Med. Biol. **49**, 1247 (2004).

[19] N. Hanna, D. Saltzman, D. Mukai, et al., J. ThoracCardiovasc Surg. **129**, 615 (2005).

[20] M. Tsuboi, A. Hayashi, N. Ikeda, et al., Lung Cancer**56**, 387-394 (2005).

[21] S.C. Whiteman, Y. Yang, D. G. Pittius, M. Stephens, J. Parmer, and M.A. Spiteri, Clin Cancer Res. **12**, 813 (2006).

[22] M.E. Brezinski, G.J. Tearney, N.J. Weissman, Heart**77**, 397 (1997).

[23] J.G. Fujimoto, S.A. Boppart, G.J. Tearney, B.E. Bouma, C. Pitris, and M.E. Brezinski, Heart**82**, 128 (1999).

[24] H. Kitabata, T. Kubo, and T. Akasaka, Heart**94**, 544 (2008).

[25] B. Wong, R. Jackson, S. Guo, J. Ridgway,U. Mahmood,J. Su, T. Y. Shibuya, R. L. Crumley,M Gu, W. B. Armstrongand,Z. Chen, The Laryngoscope **115**,904 (2005).

[26] M. T. Tsai, H. C. Lee, C. W. Lu, Y. M. Wang, C. K. Lee, C. C. Yang, and C. P. Chiang, J. Biomed. Opt. **13**, 044012 (2008).

[27] M. T. Tsai, H. C. Lee, C. K. Lee, C. H. Yu, H. M. Chen, C. P. Chiang, C. C. Chang, Y. M. Wang, and C. C. Yang, Opt. Express **16**, 15847 (2008).

[28]X. J. Wang, T. E. Milner, and J. S. Nelson, Opt. Lett. **20**, 1337 (1995).

[29] Z. Chen, T. E. Milner, S. Srinivas, X. Wang, A. Malekafzali, M. J. van Gemert, and J. S. Nelson, Opt. Lett. **22**, 1119 (1997).

[30] J. F. de Boer, T. E. Milner, M. J. Gemert, and J. S. Nelson, Opt. Lett. **22**, 934 (1997).

[31] G. Yao and L. V. Wang, Opt. Lett. **24**, 537 (1999).

[32] U. Morgner, W. Drexler, F. X. Kärtner, X. D. Li, C. Pitris, E. P. Ippen, and J. G. Fujimoto,Opt. Express**25**, 111 (2000)

[33] J. M. Schmitt, S. H. Xiang, and K. M. Yung, J. Opt. Soc. Am. A. **15**, 2288 (1998)

[34] A. M. Rollins, M. D. Kulkarni, S. Yazdanfar, R. Ung-arunyawee, and J. A. Izatt, Opt. Express**3**, 219 (1998).

[35] G. Hausler and M. W. Lindner, J. Biomed. Opt. **3**, 21 (1998).

[36] A. F. Fercher, C. K. Hitzenberger, G. Kamp, and S. Y. Elzaiat, Opt. Commun. **117**, 43 (1995).

[37] J. F. de Boer, B. Cense, B. H. Park, M. C. Pierce, G. J. Tearney, and B. E. Bouma, Opt. Lett. **28**, 2067 (2003).

[38] M. A. Choma, M. V. Sarunic, C. H. Yang, and J. A. Izatt, Opt.

Express**11**, 2183 (2003).

[39] R. Leitgeb, C. K. Hitzenberger, and A. F. Fercher, Opt. Express**11**, 889(2003).

[40] M. Wojtkowski, A. Kowalczyk, R. Leitgeb, and A. F. Fercher, Opt. Lett. **27**, 1415 (2002).

[41] S. R. Chinn, E. A. Swanson, and J. G. Fujimoto, Opt. Lett. **22**, 340 (1997).

[42] S. H. Yun, G. J. Tearney, J. F. de Boer, and B. E. Bouma, Opt. Express**12**, 2977 (2004).

[43] J. Zhang, J. S. Nelson, and Z. Chen, Opt. Lett. **30**, 1 (2005).

[44] J. Zhang, Q. Wang, B. Rao, Z. Chen, and K. Hsu, Appl. Phys. Lett. **89**, 073901 (2006).

[45] Y. Yasuno, Y. Hong, S. Makita, M. Yamanari, M. Akiba, M. Miura, and T. Yatagai, Opt. Express **15**, 6121 (2007).

[46] R. Huber, M. Wojtkowski, and J.G. Fujimoto, Opt. Express**14**, 3225 (2006).

[47] X. J. Wang, T. E. Milner, and J. S. Nelson, Opt. Lett. **20**, 1337 (1995).

[48] J. A. Izatt, M. D. Kulkarni, S. Yazdanfar, J. K. Barton, and A. J. Welch, Opt. Lett. **22**, 1439 (1997).

[49] Z. Ding, Y. Zhao, H. Ren, J. Nelson, and Z. Chen, Opt. Express**10**, 236 (2002).

[50] J. Zhang, J. S. Nelson, and Z. Chen, Opt. Lett. **30**, 1 (2005).

[51] C. Zhou, T. H. Tsai, D. C. Adler, H. C. Lee, D. W. Cohen, A. Mondelblatt, Y. Wang, J. L. Connolly, and J. G. Fujimoto, Opt. Lett. **35**, 700 (2010).

[52] R. V. Kuranov, S. Kazmi, A. B. McElroy, J. W. Kiel, A. K. Dunn, T. E. Milner, and T. Q. Duong, Opt. Express**19**, 23831 (2010).

[53] D. C. Adler, S. W. Huang, R. Huber, and J. G. Fujimoto, Opt. Express**16**, 4376 (2008).

[54] C. Zhou, T. H. Tsai, D. C. Adler, H. C. Lee, D. W. Cohen, A. Mondelblatt, Y. Wang, J. L. Connolly, and J. G. Fujimoto, Opt. Lett. **35**, 700 (2010).

[55] C. S. Kim, P. Wilder-Smith, Y. C. Ahn, L. H. L. Liaw, Z. Chen, and Y. J. Kwon, J. Biomed. Opt. **14**, 034008 (2009).

[56] J. H. Baek, T. Krasieva, S. Tang, Y. Ahn, C. S. Kim, D. Vu, Z. Chen, and P. Wilder-Smith, J. Biomed. Opt. **14**, 044001 (2009).

[57] J. Chen, F. Saeki, B. J. Wiley, H. Cang, M. J. Cobb, Z. Y. Li, L. Au, H. Zhang, M. B. Kimmey, X. Li, and Y. Xia, Nano. Lett. **5**, 473 (2005).

[58] H. Cang, T. Sun, Z. Y. Li, J. Chen, B. J. Wiley, Y. Xia, and X. Li, Opt. Lett. **30**, 3048 (2005).

[59] E. V. Zagaynova, M. V. Shirmanova, M. Y. Kirillin, B. N. Khlebtsov, A. G. Orlova, I. V. Balalaeva, M. A. Sirotkina, and M. L. Bugrova, Phys. Med. Biol. **53**, 4995 (2008).

[60] M. Kirillin, M. Shirmanova, M. Sirotkina, M. Bugrova, B. Khlebtsov, E. Zagaynova, J. Biomed. Opt. **14**, 021017 (2009).

[61] A. M. Gobin, M. H. Lee, N. J. Halas, W. D. James, R. A. Drezek, and J. L. West, Nano.Lett. **7**, 1929 (2207).

[62] A. L. Oldenburg, M. N. Hansen, D. A. Zweifel, A. Wei, and S. A. Boppart, Opt. Express**14**, 6724 (2006).

[63] K. L. Kelly et al., J. Phys. Chem. B. **107**, 668 (2003).

[64] C. F. Bohren and D. R. Huffman, John Wiley & Sons, Inc., New York, NY, 1st edition (1983).

[65] M. C. Daniel and D. Astruc, Chem. Rev. **104**, 293 (2004).

[66] M. Eghtedari, A. V. Liopo, J. A. Copland, A. A. Oraevsky and M. Motamedi, Nano.Lett. **9**, 287 (2009).

[67] W. I. Choi, J. Y. Kim, C. Kang, C. C. Byeon, Y. H. Kim, and G. Tae, ACS Nano **5**, 1995 (2011).

[68] G. von Maltzahn, J. H. Park, A. Agrawal, N. K. Bandaru, S. K. Das, M. J. Sailor, and S. N. Bhatia, Cancer Res. **69**, 3892 (2009).

[69] A. M. Gobin, J. J. Moon, and J. L. West, Internal. J. Nanomed. **3**, 351 (2008).

[70] A. M. Gobin, M. H. Lee, N. J. Halas, W. D. James, R. A. Drezek, and J. L. West, Nano. Lett. **7**, 1929 (2007).

[71] L. B. Carpin, L. R. Bickford, G.Agollah, T. K. Yu, R. Schiff, Y. Li, and R. A. Drezek, Breast Cancer Res. Treat. **125**, 27 (2011).

[72] A. M. Schwartzberg, T. Y. Olson, C. E. Talley, and J. Z. Zhang, J. Phys. Chem. B. **110**, 19935 (2006).

[73] J. Z. Zhang, J. Phys. Chem. Lett. **1**, 686 (2010).

[74] J. Chen, D. Wang, J. Xi, L. Au, A. Siekkinen, A. Warsen, Z. Y. Li, H. Zhang, Y. Xia, and X. Li, Nano. Lett. **7**, 1318 (2007).

[75] J. Chen, F. Saeki, B. J. Wiley, H. Cang, M. J. Cobb, Z. Y. Li, L. Au, H. Zhang, M. B. Kimmey, X. Li, and Y. Xia, Nano. Lett .**5**, 473 (2005).

[76] J. Chen, C. Glaus, R. Laforest, Q. Zhang, M. Yang, M. Gidding, M. J. Welch, and Y. Xia, Small **6**, 811 (2010).

[77] M. E. Brezinski, G. J. Tearney, B. E. Bouma, J. A. Izatt, M. R. Hee, E. A. Swanson, J. F. Southern, and J. G. Fujimoto, Circulation**93**,

1206 (1996).

[78] S. Y. Wu, W. M. Chang, H. Y. Tseng, C. K. Lee, T. T. Chi, J. Y. Wang, Y. W. Kiang and C. C. Yang, Plasmonics **6**,547 (2011).

[79] K.Sokolov, M.Follen, J. Aaron, I.Pavlova, A.Malpica, R.Lotan and R. Richards-Kortum, Cancer Research **63**, 1999 (2003).